Final Technical Report

Demonstrating Autonomous Control Framework Using Graphite Exponential Pile
NEUP 19-17185
Technical Workscope RC-11
12/29/2022

Bren Phillips[1*], Jiankai Yu, Jarod Wilson[1], Andrea M. Molina-Dejesus[1], Benoit Forget[1], Akshay J. Dave[2], Kaichao Sun[3]

[1]Massachusetts Institute of Technology, Nuclear Science and Engineering
[2]Argonne National Laboratory
[3]International Atomic Energy Agency

[*]Corresponding Author (bren@mit.edu)

Executive Summary

The push for small modular reactor deployment as a solution to CO_2 emissions has highlighted the need for autonomous control systems for nuclear reactor systems to minimize operational costs and minimize human error in the operation of a large fleet of modular reactors. Operational reactors are not ideal testbeds for new control systems so the MIT Graphite Exponential Pile (MGEP) was identified as and ideal testbed as it is subcriticdal with a keff of ~0.8 and is a flexible pile where instrumentation and controls can be installed and removed easily.

A dual control rod moving system that utilized two boronated control rods traveling half the length of the pile and a mobile detector was designed and fabricated. This system was controlled with stepper motors through a LabVIEW interface.

The MGEP neutronics were modeled in OpenMC and a digital twin was developed of the system. The OpenMC model was used to create simulated flux readings from a detector that were then used to train an artificial neural network developed using the open-source artificial neural network (ANN) machine learning code toolkit – NPSN. The system was trained to respond to perturbations from one of the control rods, known as the initiating control rod (ICR). The neural network would predict the location of the ICR and move the responding control rod (RCR) to the symmetric position to restore a symmetric neutron flux in the pile.

The same approach was taken with the actual control system, and the LabVIEW interface was interfaced with a neural network trained on the experimental data of various positions of the ICR and the RCR in the pile. The experimental system could then predict the location of the ICR and move the RCR to the symmetric position. The experimental system was able to predict the ICR location within about 4 cm. The digital twin system was able to perform even better by not having uncertainties in geometry, control rod position, detector position, or materials.

Fault tolerance was also investigated for the system and various methods were investigated to help identify faulty signals from the detector and replace the bad data with simulation data. The best method was able to reject 95% of the faulty signals fed to the system.

Overall the project successfully implemented an autonomous control system both using a digital twin of the MGEP and a physical autonomous control system on the actual MGEP. The digital control system was able to predict the location of an unknown movement of a control rod (ICR) and move another control rod (RCR) to a symmetric position. The symmetry of the flux was shown to be within just a little over 1% after the RCR response. Fault tolerance methods were also employed to demonstrate the robustness of the system to faulty data inputs. The project demonstrated that the use of autonomous control systems on nuclear systems is feasible.

Table of Contents

List of Figures

List of Tables

1 Introduction

Focus on the impacts of increasing CO_2 emissions naturally increases the attractiveness of nuclear power generation technology. Indeed, next-generation micro and modular nuclear reactor technology has seen renewed interest. Still, future nuclear power plant designs will need to simultaneously make advances in operation methods in order to be cost-competitive against other electricity generation technologies [1]. One avenue being pursued to accomplish such strides is towards the development of fully autonomous reactor control systems [2]. The recent explosion in performance and range of Machine Learning (ML) algorithms seen in other fields appears ripe for application to such autonomous control systems. Nonetheless, the high degree of safety required for nuclear plants precludes the possibility of testing and developing nascent ML-driven control frameworks on existing fission systems. To bridge this gap the MIT Graphite Exponential Pile (MGEP) has been identified for the development of a novel, first-of-a-kind demonstration of the autonomous control of a nuclear reactor. Importantly, the subcritical nature of the pile eliminates the danger of significant radionuclide release resulting from unexpected behaviors while such a control system is in use.

Autonomous control systems (ACS) have recently seen increased use in many industries with the rapid development of artificial intelligent (AI) technologies, including machine learning algorithms and their different realizations with multi-layer neural networks. The rapid deployment of digital instruments and sensors during the operation of nuclear power plants (NPPs) has also inspired the interest of ACS. The emerging advanced nuclear energy systems, such as space reactors, small modular reactors (SMRs), and even micro-reactors, provides additional demand for ACS due to the requirement of inherent safety without human intervention from the start of conceptual design to the final operation and maintenance.

1.1 Motivation

Autonomous control is a key technology for Special Purpose Reactors R&D. It assists reactor operation with enhanced safety and reliability under normal and off-normal (accident) conditions. More importantly, such technology could help in reducing the operational cost. The proposed research aims to develop a detection-prediction-feedback (DPF) framework for a nuclear system autonomous control (see Figure 1). Three key components in this framework are: 1) a mobile detector that will be placed in the nuclear system and perform online measurements, 2) a prediction model that will utilize measured data as input to derive computational solutions for decision-making algorithms, 3) control feedback that will be enabled as real-time response to any unknown initiating events and such a response will satisfy certain pre-defined criterion.

Figure 1: Detection-prediction-feedback framework for demonstrating nuclear system autonomous control

In addition to the methodology development of autonomous control, the proposed research project will entail a first-of-a-kind engineering demonstration on a real nuclear fission system. The in-house university MIT Graphite Exponential Pile (MGEP) has been selected for such a task. This facility was recently restarted. It is now fully operational and readily available for internal users.

1.2 Previous Work

Several previous works have introduced autonomous control system designs, specifically for nuclear energy. Upadhyaya et al. [3] proposed an autonomous control system based on a space reactor to perform fault detection using the principal component analysis. Lin et al. [4] proposed an autonomous operation algorithm to prevent core damage from severe accidents such as loss of coolant accidents, and steam generator tube ruptures in commercial pressurized water reactors. Lin et al. [5] proposed the so-called Nearly Autonomous Management and Control (NAMAC) system that is purported to offer the operators recommendations on how to maintain both operational safety and reactor core performance. NAMAC is composed of a knowledge base, digital twin (DT), and operational workflow. These works indicate that an ACS for neutronic reactivity control is rarely developed for nuclear facilities. Additionally, the machine learning based kernel of these autonomous control systems are completely trained and demonstrated by simulation data from high-fidelity numerical modeling and/or simulators. The challenging issue that occurs in experimental demonstration of neutronic reactivity-based ACS or NACS is from the lack of accessible experimental data with changes in reactivity control mechanisms.

The Massachusetts Institute of Technology (MIT) Nuclear Reactor Laboratory (NRL) has a graphite exponential pile (MGEP). The pile uses natural uranium as the fissile material and nuclear grade graphite as the moderator. The geometric layout and material composition were intentionally designed to be subcritical with an effective multiplication factor (k_{eff}) of approximately 0.8. Thus, an external neutron source is needed to produce a measurable neutron flux. Therefore due to the inherent safety, the MGEP serves as an excellent test bed for research, education, and demonstration use [2], [6]–[15].

2 Design and Fabrication of the MGEP control system

2.1 MIT Graphite Exponential Pile Facility Background

The MGEP is a subcritical nuclear reactor constructed from graphite and natural uranium. Built with surplus nuclear-grade graphite not needed for the construction of the MIT Reactor (MITR-I), the MGEP was initially erected in 1957 to serve as an experimental facility for the Department of Nuclear Engineering. The MGEP saw intermittent use through 1991 but sat underutilized for much of its life. In 2016, now-retired Professor Kord Smith oversaw the revival of the MGEP as an experimental and educational resource for both the Nuclear Reactor Laboratory (NRL) and Department of Nuclear Science and Engineering (NSE).

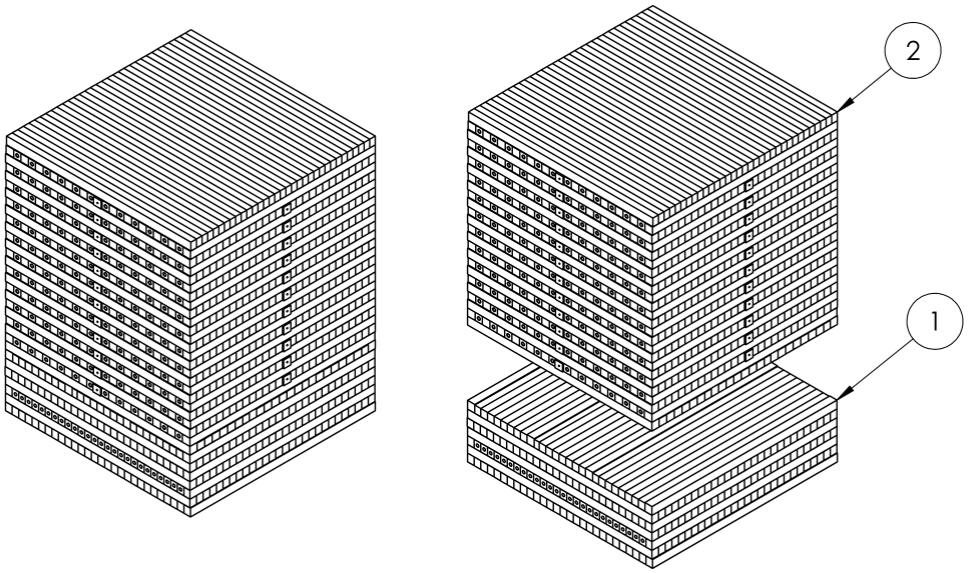

Figure 2: Engineering drawing of the MIT Graphite Exponential Pile (MGEP) experimental facility. The diagram on the left shows the real-world configuration of all graphite moderating blocks in full, whereas the diagram on the right visually separates the Lower Pedestal (1) from the Fuel Lattice (2) [6]**.**

The MGEP consists of two sections, shown in Figure 2, where both sections are constructed from alternating layers of perpendicular graphite moderating blocks. The Lower Pedestal (LP) is a below-grade lattice, which has twenty-six channels available to house an external neutron source.

The above-grade Fuel Lattice (FL) serves as the primary section of the pile used for this project. Standing as a square cube roughly measuring 90 inches each side, the FL is highly configurable for experimentation. 144 fuel channel graphite blocks arranged in a 12x12 grid run the North-South orientation of the pile. These channels are typically loaded with aluminum-clad natural uranium fuel slugs, and any combination of channels can be de-fueled to serve as an insertion point for instrumentation. The same fuel channel blocks run half the length of the East-West oriented blocks. In addition, any graphite block in its entirety can be removed from the lattice structure, thus allowing even greater freedom in instrumentation and control system design [6].

The initial motivation behind the revival of the MGEP was its design as a subcritical nuclear reactor that could be used as an educational tool for the MIT community. Additionally, the inherent safety and high degree of configurability of the pile make it an ideal testbed for novel ML-based control systems. Several undergraduate theses completed the initial work necessary to demonstrate the viability of the MGEP as such an experimental facility. Starting in 2018, the basic characterization of the pile was compiled; beyond geometry and construction, the neutron flux within the FL was experimentally obtained via foil activation [6]. Building on this in 2019, Monte Carlo modelling of the pile was completed, determining $k_{eff} \approx 0.8$ for a fully-fueled pile [7]. In the same year, an undergraduate-level investigation applied rudimentary ML methodology to reconstruct the neutron flux of the pile and began initial fabrication of the control components used for this project [8].

In summation, the MGEP experimental facility serves as the perfect platform on which to develop a ML-driven autonomous control testbed. The layout and construction of the FL allows for great freedom in experiment design, particularly in relation to the positioning of instrumentation and control devices. Additionally, this project builds on a body of work that highly supports its use as a full-fledged experimental facility. Most importantly, because it is a subcritical facility, the MGEP can be used to safely demonstrate a first-of-a-kind, ML-driven autonomous control system.

2.2 Design Considerations

Because it is a subcritical facility, the MGEP possessed limited functionality regarding flux measurement and control systems. After its restart in 2016, measurements of its characteristics were conducted through the previously discussed foil irradiation experiments, or via three He-3 neutron detectors. Physical control of pile characteristics was accomplished by altering the physical configuration of the pile, either by rearranging the fuel loading pattern, or by varying the location and type of external neutron source. Aluminum control rods containing Shieldwerks SWX-237Z30, a castable boron-silicon material, were manufactured for the pile as well. Regarding the wider effort to use the MGEP as a ML testbed, both the detectors and control rods will be referred to as Control Devices (CDs).

While useful for basic experiments, positioning of the existing CDs within the pile was static unless manually altered by hand. Such limited operation is not suitable for the stated goal of demonstrating real-time, autonomous control. In response, a facility-specific Detector and Absorber Linear Motion Assembly (DALMA) was developed and will be installed within the MGEP. The DALMA was tailor-made both to meet the requirements of the higher-level Graphite Pile Control System (GPCS), as well as function within constraints uniquely posed by the pile.

2.2.1 Experiment and Graphite Pile Control System Requirements

A schematic of the preliminary layout for control devices within the MGEP can be seen in Figure 3. Because the experiment design aims to measure and control the neutron flux within the pile in one axial direction, movement of CDs in a DALMA can be similarly restricted; channels running in the East-West orientation of graphite blocks were selected for use. A He-3 detector on a mobile rail was used. Additionally, two neutron-absorbing CDs were required, each operating over half the length of one channel. For operation, all CDs must be able to move independently of one another. Additionally, the higher-level control logic and ML models require that the position of CDs relative to their location in the pile is highly precise; ±1mm. As part of the concurrent work to develop the GPCS, a LabVIEW system was developed in tandem (discussed din later sections) to handle decision-making logic and a CD positioning interface. Components used in the DALMA were selected with compatibility in mind.

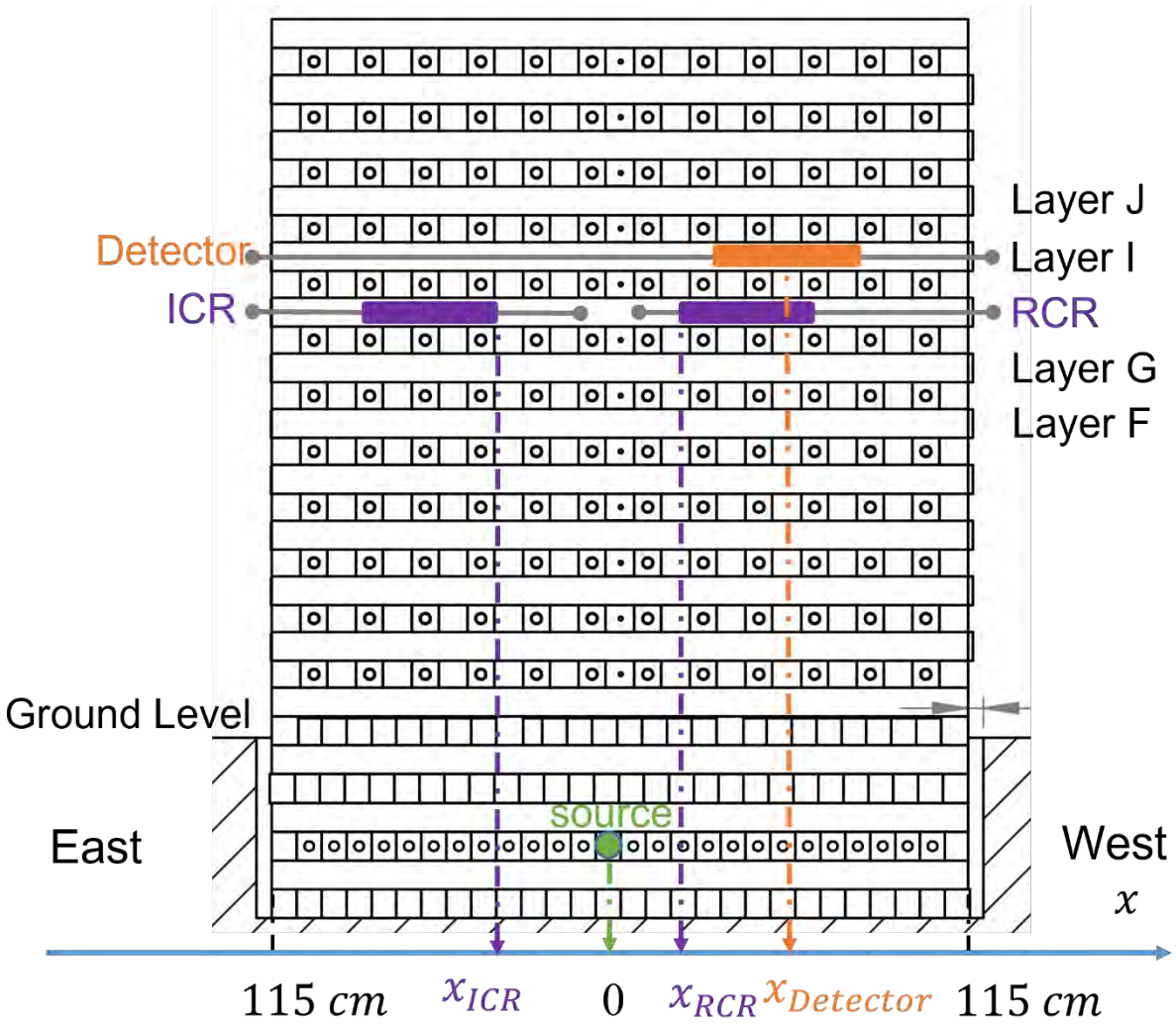

Figure 3: Front View of MGEP modeling

2.2.2 Facility Limitations and Considerations

Some limitations were imposed on DALMA design due to MGEP characteristics. Neutron flux within the pile is relatively small. Therefore, the absorption cross-section of the materials used was kept in mind. Such consideration aimed to both limit the activation of components inserted into open channels of the MGEP and minimize unnecessary interference with the neutron flux. As such, large structural components of the DALMA are made of aluminum.

More significant restrictions on the design of the DALMA were created by the pile's geometry and security procedures. The graphite block channels intended to house the position control assemblies measure 3.5 inches in width and 3.75 inches in height. Both the He-3 detectors and control rods measure roughly 1-inch in diameter, leaving limited space for components necessary to mechanically move them through the pile. Additionally, because the experimental setup aims to house all DALMAs within three concurrent EW-oriented graphite block channels, components located outside of the pile were limited in potential overall height. Finally, the operating security procedure of the MGEP facility created unique design constraints for the DALMA. When the pile is loaded with its natural-uranium fuel, it may not be left unsecured – the locking covers which

surround all four faces must be in place. Any permanently installed system would thus require the unloading and loading all 1,288 slugs any time the pile was not manned. More realistically, any installation of CDs must be able to be at least partially assembled and deconstructed. This restriction complicated both the DALMA's ease of use and ability to operate precisely.

2.3 Linear Motion Assembly Description and Specifications

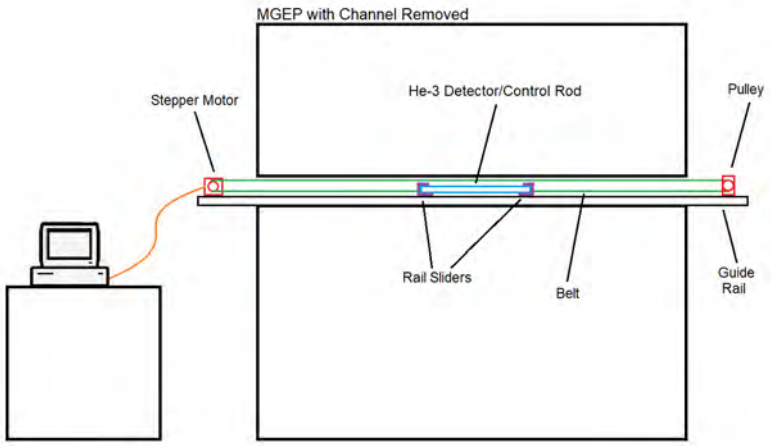

Figure 4: A generalized DALMA running the full length of a removed channel within the MGEP.

To meet experimental requirements and constraints, the DALMA was selected to be a synchronous belt-driven system operated over T-slotted rails, controlled by a high-torque stepper motor. Both the He-3 detectors and neutron-absorbing control rods fit into sliders, which are attached to the driving belt. Figure 4 shows the basic components and design one assembly. Each DALMA can be independently controlled over a fixed length, currently set to be either the full or half length of the removed channel. Movement is accomplished through a single stepper motor and belt loop, with the end opposite the motor housing idler pulleys. Each DALMA will connected to a centralized computer, which will operate the GPCS and is powered externally via 24 V power supplies.

A belt-driven system powered by a stepper motor provides several key benefits necessary for the precise linear movement of control components within the pile. Stepper motors are widely used for a variety of purposes, and as such come in a variety of performance specifications. Additionally, stepper motors are highly precise. Using structural rail framing for both mounting of the stepper/pulley sub-assemblies as well as a guide for the CDs allows the system to be more modular – operating length of a DALMA can be altered by simply changing the mounting location of the idler pullies and belt length. Additionally, the guide rail eliminates the possibility of off-axis movement. Finally, the described design characteristics minimize the use of custom in-house parts, by implementing off-the-shelf electronic and mechanical components wherever possible. Components that were built in-house were mostly manufactured from 3D-printed PLA plastic, allowing faster iterative development and production.

2.3.1 Component Housing and Rail Slider Schematics

3D renders of the DALMA sub-assemblies can be seen in Figure 5 & Figure 6. Table 1 contains further description of the individually labeled components. Each DALMA's components can grouped into three main categories; guide and support framing, electronic and mechanical pieces, and 3D-printed housing fixtures made from 100% infill PLA. The entire designs shown below, and their subsequent fabrication, were completed in-house, specifically to support efforts to demonstrate autonomous control. However, whenever possible, off-the-shelf components were selected in order to minimize complexity and overhead. All of the structural rail pieces are standard 30 mm T-slotted aluminum framing, widely available and used in lab settings. Electronic and mechanical parts were also selected from common-spec options; the belt and pulleys are standard 2GT spec – commonly found in 3D-printer applications. Utilizing 3D-printing technology to produce the housing components allowed for fast, low-cost iteration of the overall design and rapid production of finalized parts. Indeed, these pieces were re-designed and tweaked many times, to improve overall system rigidity, precision, ease-of-use, and modularity.

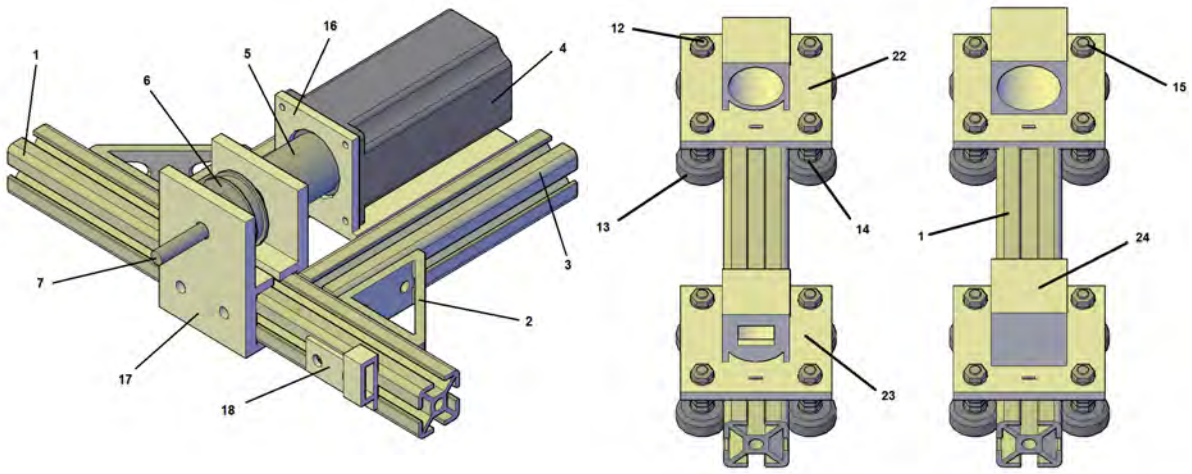

Figure 5: Motor housing sub-assembly and sliders. The left image shows a render of the motor sub-assembly, and the right image shows the sliders used to house the He-3 neutron detector and control rods. Corresponding figure labels are found in Table 1.

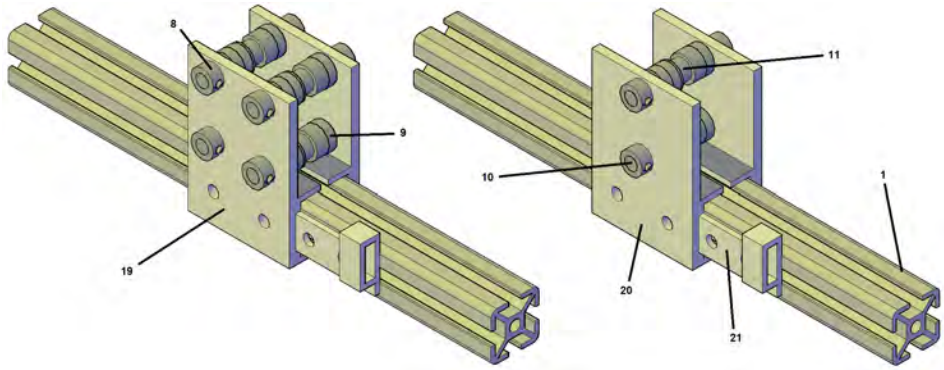

Figure 6: Idler pulley housing sub-assemblies for single and dual-CD DALMAs. The left render shows the idler pulley housing for a dual-CD DALMA and is attached to the center of the guide rail. The right render shows the pulley housing for a single-CD DALMA and is attached to the end of the guide rail. Corresponding figure labels are found in Table 1.

Table 1: Sub-assembly component label guide

Label Number	Component	Label Number	Component
1	10 ft Guide Rail	**13**	Chamfered Rubber Guide Bearing
2	Structural Gusset	**14**	M5 Washer
3	7 in Mounting Rail	**15**	M5 Nut
4	NEMA23 Stepper Motor	**16**	Stepper Motor Mount
5	8 mm to 10 mm Shaft Couple	**17**	Drive Housing w/ Bearing
6	42 mm OD 2GT Pulley	**18**	Limit Switch Housing
7	8 mm Drive Axle	**19**	Dual CD Pulley Housing
8	8 mm Clamp Collar	**20**	Single CD Pulley Housing
9	16 mm Bearing	**21**	Limit Switch Housing
10	8 mm Pulley Axle	**22**	He-3 Detector Slider
11	16 mm OD 2GT Pulley	**23**	He-3 Detector Slider w/ ETH Port
12	M5 35 mm Bolt	**24**	Control Rod Slider

The position of each CD will be individually controlled via a single belt loop driven by a NEMA23 high-torque stepper motor. The motor is controlled via a STEPPERONLINE DM542T driver, which in turn receives input 5 V signals for motor direction and speed from a programmable board. A rendered image of a mounted motor can be seen in the left side image of Fig 5. The motor itself is secured to a 3D-printed mounting piece which is bolted between two 7-inch structural rail frames which are orthogonal to the end of the guide rail. The drive shaft of the motor is coupled to an 8 mm axle, which supports a larger 2GT pulley. In a slightly novel printing process, bearings have been imbedded into the 3D-printed motor housing pieces, to reduce friction and drag on the drive axle during operation.

Because the experimental setup requires that a variable number of CDs be configured in half-length and full-length channels of the MGEP, two separate pulley housings were necessary. Both are similar, and share basic components, as can be seen in Figure 6. Both are designed to sit opposite the motor sub-assembly for a CD, looping the belt back towards the corresponding slider. The pulley sub-assembly on the left side of Fig. 6 is for a dual-CD DALMA setup. As such it houses four smaller 2GT pulleys and is mounted in the middle of the guide rail. The right-side image of Fig. 6 shows the pulley sub-assembly for a single-CD configured DALMA, which only contains two 2GT pulleys. Because this housing is for a full-length configuration, it is affixed to the end of the guide rail opposite the driving motor. The pulleys within these sub-assemblies spin freely with the drive belt, and as such the 8 mm axles are stationary, locked in place via clamp collars attached to the outer face of the 3D-printed housing pieces. These axles are machined to 60 mm in length to fit within the channel width.

The CDs themselves sit within 3D-printed sliders, which allow motion over the guide rail. The slider designs for both the He-3 neutron detector and the control rods are very similar, as can be seen in Fig 6. Due to physical specifications, the detector sliders are slightly smaller. In addition,

one slider piece for the He-3 neutron detector has a through-port to allow the power and data-transfer ethernet cable to be connected. All sliders are fitted with chamfered rubber bearings which sit on the side channels of the guide rail. These bearings allow the CDs housed within the slider pieces to smoothly glide in line with the guide rail. The sliders also have two 5 mm holes where the drive belt is affixed, thus completing the belt loop. Fig. 7 shows a functioning DALMA with a He-3 neutron detector inserted, as well as a dual-CD DALMA during assembly.

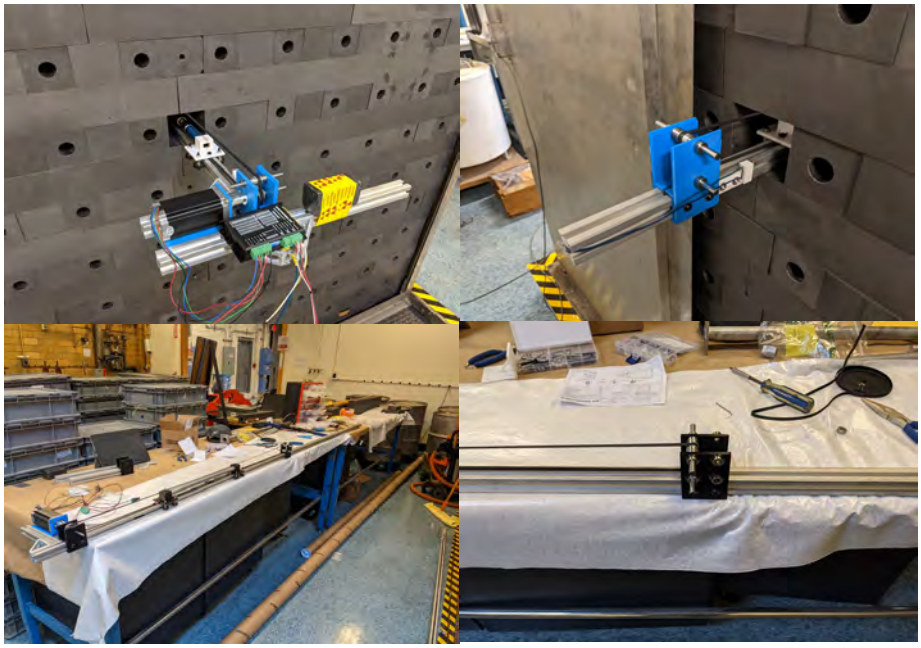

Figure 7: From left to right, top to bottom; motor sub-assembly of a DALMA inserted into the MGEP, pulley sub-assembly of a DALMA inserted into MGEP, dual-CD DALMA partially assembled out of pile, dual-CD pulley sub-assembly with belt attached in one direction.

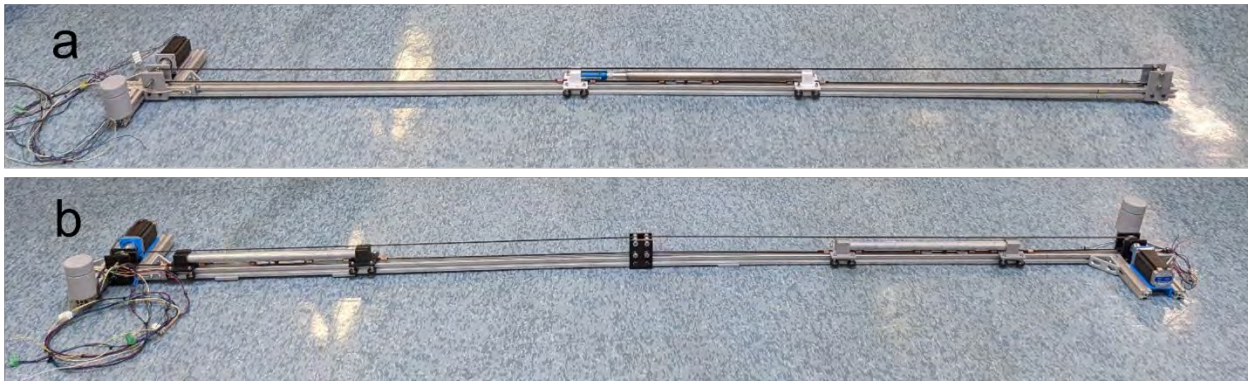

Figure 8: Hardware fabrication a) detector moving system; b) dual control rods moving system.

1.1 Positioning Calibration Procedure

Because the MGEP must be secured via sheet metal covers when not in use, any experimental facilities developed for it much be removed should they extend beyond any face of the pile. For the DALMAs, this means they must be partially disassembled between experiments. However, due to doors on the sides of the panels through which the rails pass, it was possible to midify the doors to allow the covers to be in place, and locked whiel the rails are inserted. Thus, the need to remove the rails after every experiment was avoided for much of the project. Because high precision is necessary, calibration of the system is needed. As their design was completed and built in-house, a software-based calibration procedure was also developed. For every CD, limit switches are attached to the guide rail via 3D-printed housing pieces on either end of the belt. They are mounted in a way such that the outer edges of the sliders will trigger the switch when the CD reaches the minimum and maximum travel positions of the DALMA. The distance between these positions is accurately measured and assumed to be a fixed value. Using a Python script, the number of steps taken by the motor to move the CD between the minimum and maximum position is counted. With these two values, an accurate unit distance travelled per step is determined, thus allowing precise position control of the CD. Position precision after calibration is ±1 mm.

3 MGEP Digital Twin and the Virtual Control System

A virtual control system has been developed in this project to theoretically demonstrate the autonomous operation of the MIT Graphite Exponential Pile (MGEP). The system is designed to autonomously respond to perturbations through linear actuation of control rods with neutron poisons. In this system, the unknown perturbation from a control rod position change is modeled and simulated by Monte Carlo neutron transport code -- OpenMC and then analyzed by a well-trained neural network (NN) to provide a regression model to predict the unknown control rod perturbation. And the responding control rod is then actuated to minimize the object function.

Afterwards, the virtual control system has been integrated with hardware to develop the experimental control system on the pile. In this system, the unknown control rod perturbation is captured by three to four Helium-3 neutron detectors at different spatial positions in the pile. Similarly, NN-based regression model is previously trained by the experimental data collected from Helium-3 neutron detectors. And the responding control rod is finally actuated to keep the neutron flux symmetric along the control rod direction.

The virtual control system has been developed using LabVIEW-based graphical programming language, and has integrated three major components: a neural network surrogate model to generate neutron flux detector signals, a neural network regression model to predict the target position of the unknown control rod, and a module to input unknown control rod movement.

This section describes the verification of the control system by evaluating the minimization of the steady-state and transient error, and investigating system stability.

The neural network models will be trained by the numerical data obtained from OpenMC. Finally, optimized in-pile configuration of neutron detectors will be present to achieve the good regression results with acceptable accuracy.

3.1 Modeling and Simulation

The training data sets which are used to train neural network in virtual control system are generated by the modeling and simulation with Monte Carlo neutron transport code – OpenMC [16].

Figure 3 illustrates the front view of the high-fidelity modeling of MGEP, which is a subcritical facility and has been considered as an excellent test bed for the experimental demonstration of nuclear reactor physics.

As shown in the figure, the neutron fluxes of interest are referenced relative to the graphite layers spanning from “F”, “G”, “I” and “J”. Neutron detectors may be placed in these channels to characterize the in-pile neutron flux distribution. The exact locations of neutron detectors will be adjusted to achieve optimal performance of neural network prediction models used in the virtual control system. In order to perturb the neutron flux distribution in four layers of interest, an in-pile facility has been developed to actuate linear motion of two control rods, which are the initiating control rod (ICR) and responding control rod (RCR) that are placed in the graphite "Layer H".

The high-fidelity modeling of MGEP has been validated by the comparison of simulated results with the experimental data, which is presented in the Figure 9 with two control rods being fully placed out of the pile. The simulation of OpenMC has been performed with 3.0×10^8 particles, in order to ensure that the tallied neutron fluxes have no bigger than 1% statistical uncertainty. The mesh size of the flux tallies for these four layers of interest is 2.5 cm, and a total of 90 nodes are adopted. The resulting OpenMC output tallies are a 90x4 matrix, which is the input matrix for the surrogate model.

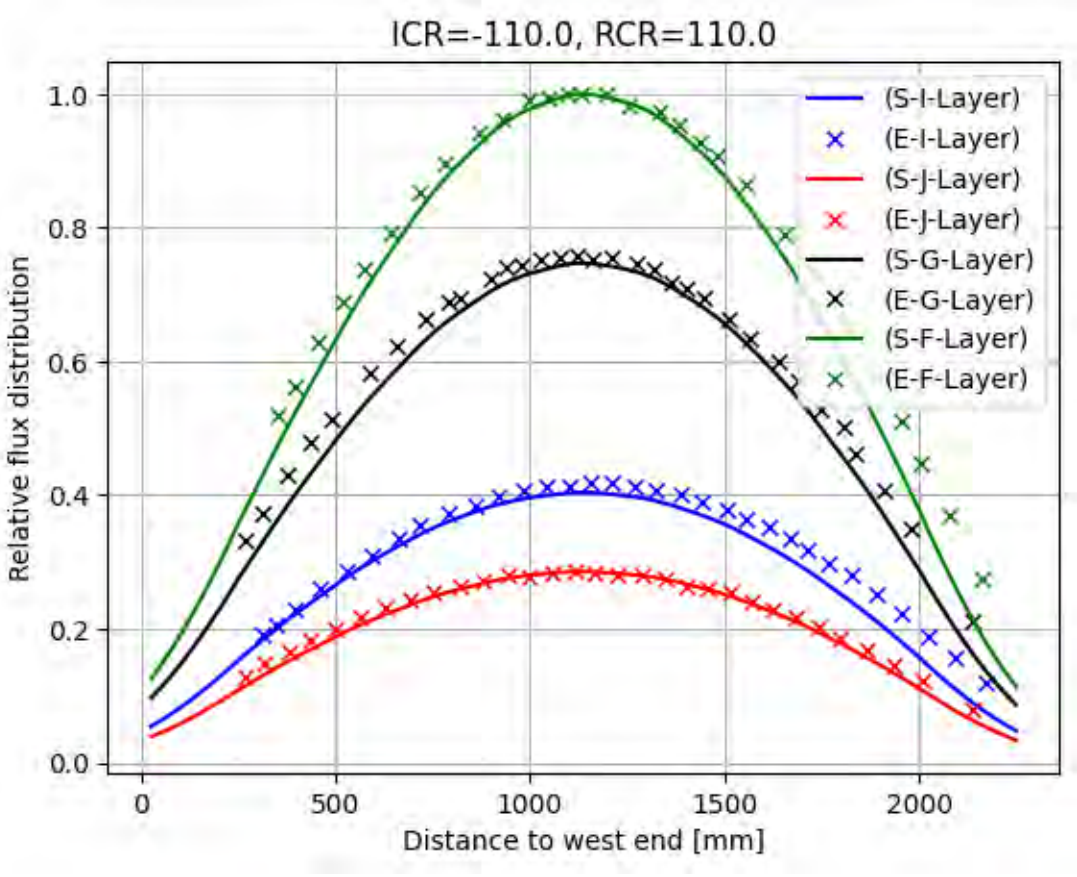

Figure 9: Comparison of simulation results with experimental data without control rod insertion. Lines are simulation results; data points are experimental data.

3.2 Artificial Neural Network

The open-source artificial neural network (ANN) machine learning code toolkit – NPSN [8], [14] has been adopted and modified to build a neural network surrogate and regression model. NPSN provides an abstract path for creating models for multidimensional regression of neutron flux distribution based on control rod position(s) for any type of nuclear reactor. The flow chart for the process is shown in Figure 10.

Two neural networks ("NN-S" and "NN-CR") are integrated into the virtual control system. The surrogate model ("NN-S") generates simulated detectors signals in the graphite pile channels of interest; and the regression model ("NN-CR") predicts the perturbed ICR position.

These two neural network models in virtual control system can be expressed in the equations below.

$$f_{NN-S} \sim f(x_{RCR}, x_{ICR}^{actual}) = \phi(d_1, \ldots, d_M)$$

$$f_{NN-CR} \sim f(\phi(d_1, \ldots, d_M), x_{RCR}) = x_{ICR}^{predicted}$$

where x is the position of control rod, φ denotes the detector signals reflecting neutron flux of the graphite pile, and M is the maximum number of measurement points. To quantify the performance of both neural network models, the relative difference in the surrogate model and the prediction error in regression model are calculated via the equations below respectively,

$$\delta_{NN-S} = \frac{\phi(d_1, ..., d_M)^{predicted} - \phi(d_1, ..., d_M)^{actual}}{\phi(d_1, ..., d_M)^{actual}}$$

$$\delta_{NN-CR} = x_{ICR}^{predicted} - x_{ICR}^{actual}$$

where $\delta_{NN\text{-}S}$ is the relative difference of NN-S model, and $\delta_{NN\text{-}CR}$ represents the prediction error of control rod perturbation in the NN-CR model.

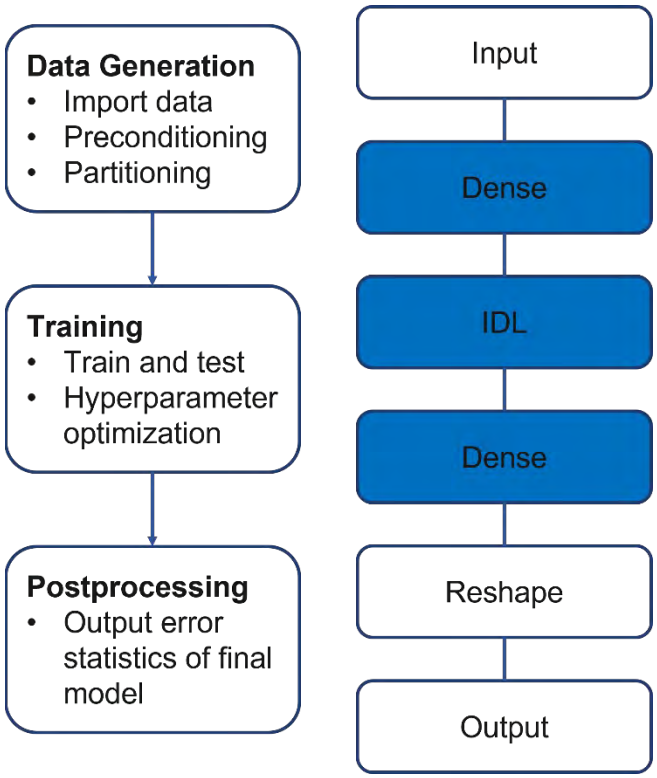

Figure 10: Flow chart of the neural network

3.3 Performance Optimization

The prediction accuracy of this virtual control system is highly dependent on the detailed locations of three low-fidelity detectors and/or one high-fidelity detector. Results of numerical testing have demonstrated that the more detectors that are close to the control rods result in better prediction accuracy.

This section elaborates the performance optimization by taking the high-fidelity detector with an active length of 100 cm, considering the 2.5 cm grid in the OpenMC model, this yields 40 points

of detector data that will be adopted as the input of NN-CR regression model. The same data set from the OpenMC simulation is used to train the NN-CR regression model, but the only exception is that greater than or equal to 40 points of detector information corresponds to mesh locations covering the high-fidelity detector location at the graphite layer of interest, and are utilized as the input to the NN-CR regression model. The optimized parameters used to train the neural network are shown in Table 2.

Table 2: Optimized architecture parameters for the neural network regression model.

Parameters	Values
Number of intermediate dense layer	3
Activation function	ReLU
Shape of intermediate dense layer	1080
Loss function	Logcosh
Optimizer	Adam
Batch size per epoch	8

The naming convention in Table 3 follows *L[x]H[y]-z*, in which *H* denotes high-fidelity detector; *L* means low-fidelity detectors; *x* is the number of *H* detectors, ranging from 0 to 1; *y* is the number of *L* detectors, ranging from 0 to 3; *z* is a unique permutation identifier, ranging from *a* to *z*. Similarly, the naming convention of detector locations can be expressed as (X, a~b~c), where *X* denotes graphite layer identifier, *F*, *G*, *I* or *J*; *a* is the starting index of detector location, ranging from 1 to 90 (total number of computational nodes in each graphite layer); *b* is the end index, ranging from 1 to 90 and equals to 1 if ignored; *c* is the interval of meshes from detector signals collection, ranging from 1 to 90 and equals to 1 if ignored.

As listed in Table 3, ten cases are primarily selected to conduct the comparative study on the optimization of the NN-CR neural network. Case 1 represents three low-fidelity detectors in the I layer, which performs the best without any high-fidelity detectors. The good performance is because the neutron flux shape of I layer reflects the most impact of control rods movement in the H layer, and this is also the reason why all other cases apply D_4 in the center of I layer. However, case 2 just adopts a high-fidelity detector in the center position. The cases starting from #3 to #10 tabulate different combinations of low-fidelity and high-fidelity detectors. Cases 3, 4 and 5 take two low-fidelity in two ends positions of I layers, as the center position of I layers has been captured by the high-fidelity detector. Cases from 6 to 10 cover different combination of three low-fidelity detectors in I and J layers with different locations in I layers. Case 10 changes the one low-fidelity detector from center position to left-tilt position in order to capture the ICR control rod movement more accurately.

Table 3: Combination of different detectors in the regression model

Case #	Name	Locations of Detectors			
		D_1	D_2	D_3	D_4
1	L3H0-a	(I, 5)	(I, 44)	(I, 85)	—
2	L0H1-a	—	—	—	(I, 26~65)
3	L2H1-a	(I, 20)	—	(I, 70)	(I, 26~65)
4	L2H1-b	(I, 10)	—	(I, 80)	(I, 26~65)
5	L2H1-c	(I, 5)	—	(I, 85)	(I, 26~65)
6	L3H1-a	(I, 5)	(J, 44)	(I, 85)	(I, 26~65)
7	L3H1-b	(J, 5)	(J, 44)	(J, 85)	(I, 26~65)
8	L3H1-c	(I, 10)	(J, 44)	(I, 80)	(I, 26~65)
9	L3H1-d	(J, 10)	(J, 44)	(J, 80)	(I, 26~65)
10	L3H1-e	(I, 5)	(J, 20)	(I, 85)	(I, 26~65)

3.4 LabVIEW Design for the Virtual Control System

The virtual control system is designed in the LabVIEW graphical programming language due to its advantage in the functional compatibility with various software, hardware, and operating systems. Figure 11 displays the front panel of this virtual control system, which contains three major components and a visualization display. The main components are the initiating control rod perturbation (ICR), responding control rod manipulation and feedback (RCR), detector signal generator and unknown control rod perturbation prediction. Two neural networks are introduced to realize the functionality behind the detector signal generator and control rod prediction. As mentioned above, NN-S and NN-CR are separately trained to support the detector signals generator and control rod prediction respectively, with the training data sets generated by high-fidelity Monte Carlo neutron transport modeling and simulations. The predicted control rod position will be finally fed back to the responding control rod manipulation.

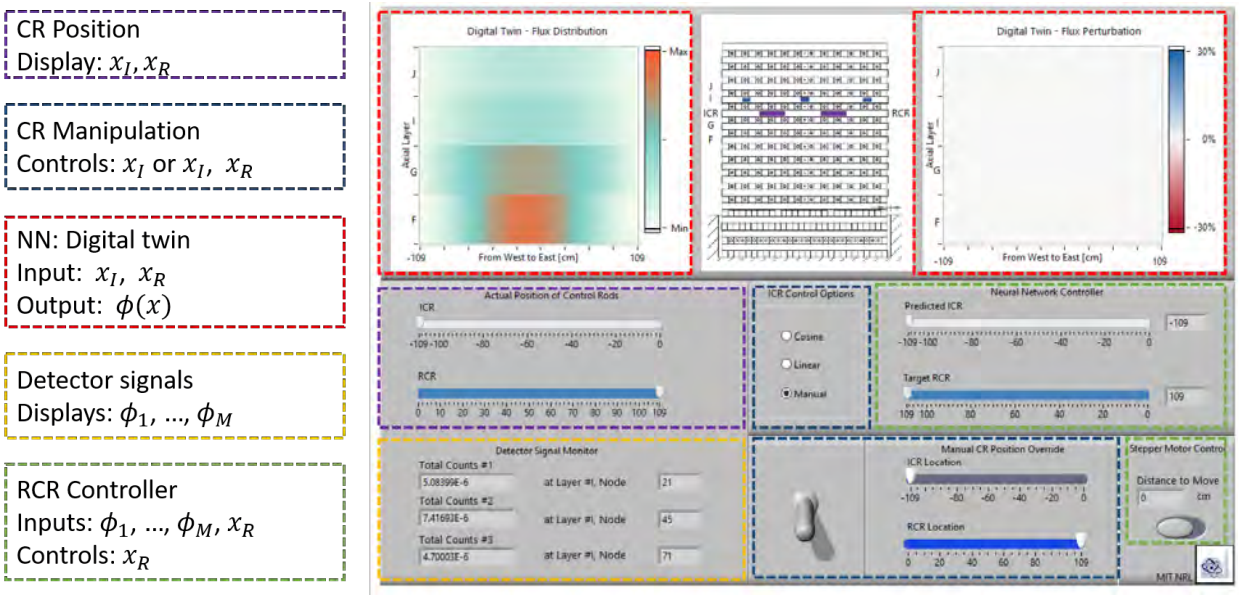

Figure 11: LabVIEW front control panel for the virtual control system

A series of training data has been adopted to train the neural network NN-S and NN-CR, which covers 142 different permutation of ICR and RCR positions and are available in Appendix A.

3.5 Regression Model Performance

The overall performance of the virtual control system is mostly determined by the performance of NN-CR regression model. The accuracy of predicting the unknown ICR perturbation is calculated by the difference between the actual ICR position and the predicted position. The testing results of all 10 permutations of detectors from Table 3 are presented in Figure 12.

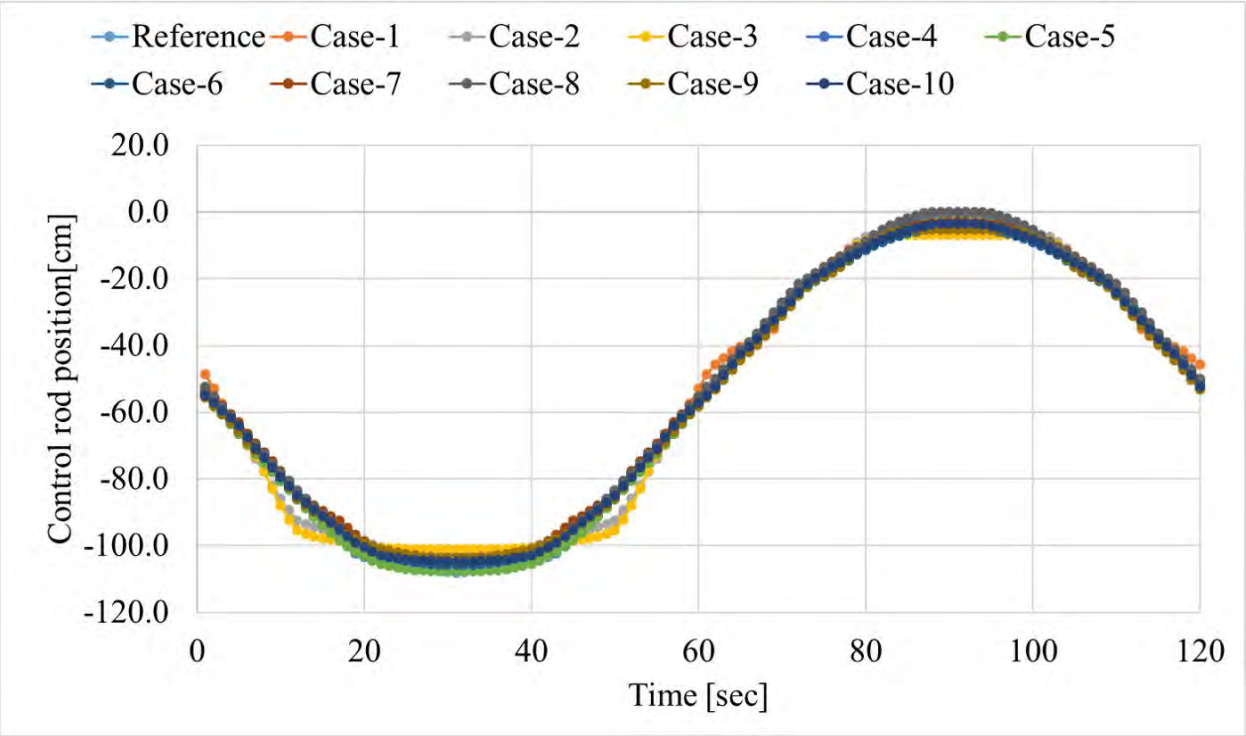

Figure 12: Performance of NN-CR regression model across different detector position/type permutations.

The testing results indicates that Case 1, 2, and 3 do not have good performance to smoothly predict the ICR sine shaped perturbation, particularly in the case that the ICR is extremely close to the ends of the graphite layer. Note that RCR position is 50 cm for all testing cases.

Figure 13 shows the detailed absolute difference of the prediction in all testing cases, which error lies within the range from approximately -15 cm to 10 cm. The results of case 2 and 3 are not acceptably accurate because of the scale of maximum error. Case 1 results are poor as the predicted ICR movement shape is not smooth. Furthermore, looking into the detailed maximum prediction error, case 5 performs the best and is analyzed further.

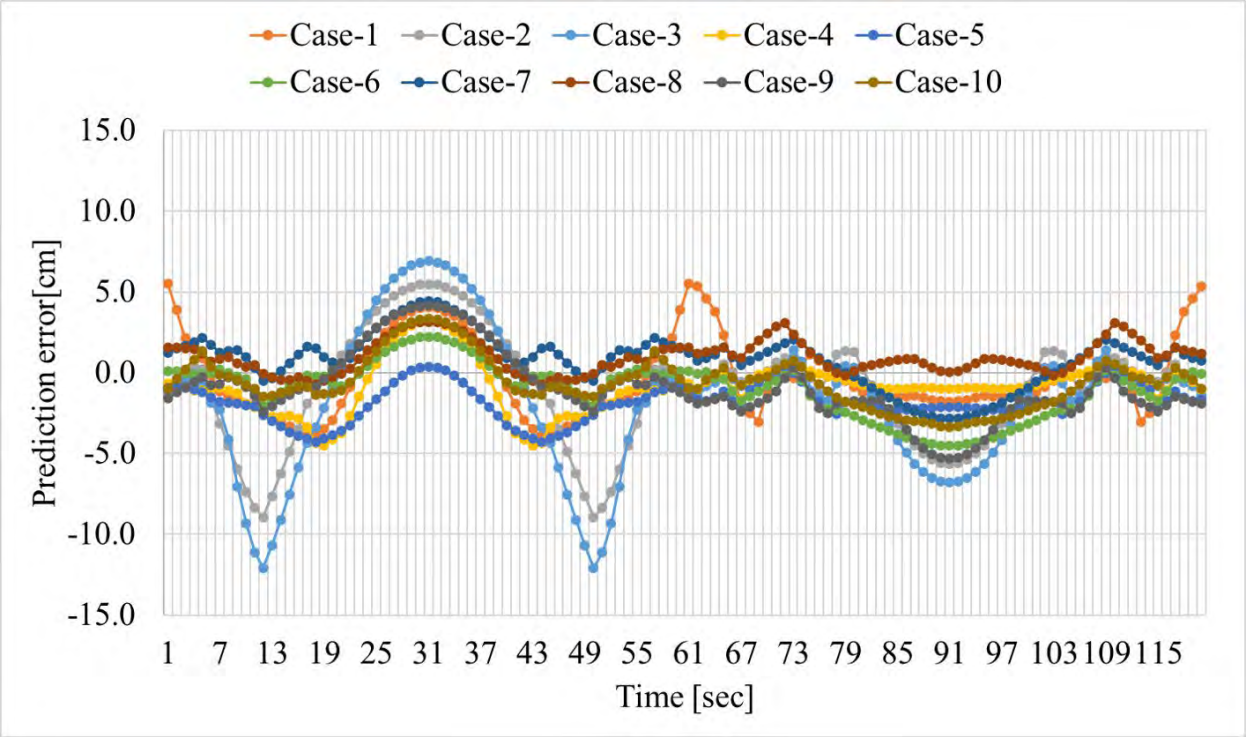

Figure 13: Performance of the virtual control system for the various cases across different times (i.e. ICR positions).

As the current position of RCR might have an impact on the NN-CR prediction performance, the sensitivity analysis of case 5 is conducted among different RCR positions. The analysis result is shown in Figure 14, where less than 5 cm of the maximum error is observed in the extreme RCR positions (RCR=100 cm or RCR=10 cm). However, the other RCR positions have even better accuracy with errors ranging from -3 cm to 1 cm. The mean absolute error, maximum absolute error, and root mean square error are provided in Table 4 for all ten test cases.

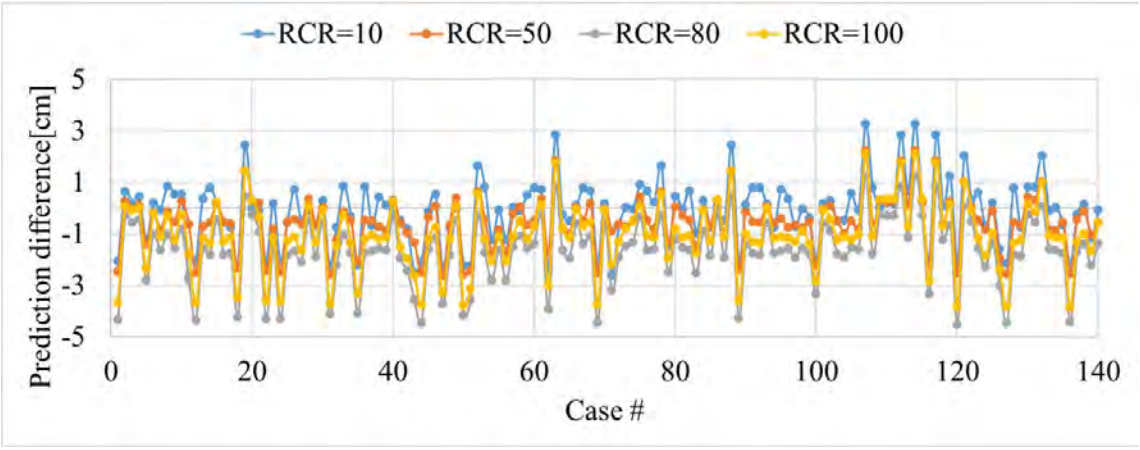

Figure 14: Optimized performance of unknown perturbation for case 5 for various RCR positions.

Table 4: Prediction error in the regression model for all cases

Case #	Name	Mean absolute error (cm)	Max absolute error (cm)	Root mean square error (cm)
1	L3H0-a	2.0	5.5	2.4
2	L0H1-a	2.6	8.9	3.4
3	L2H1-a	3.3	12.1	4.3
4	L2H1-b	1.4	4.5	1.6
5	L2H1-c	1.9	4.3	1.1
6	L3H1-a	1.4	4.5	1.7
7	L3H1-b	1.5	4.4	1.1
8	L3H1-c	1.1	3.2	1.0
9	L3H1-d	1.9	5.3	2.1
10	L3H1-e	1.3	3.4	1.6

The regression model was further optimized for case 5, and the optimized results are shown in Figure 15, where the unknown ICR perturbation is assumed has the triangle sine function shape with a period of 120 seconds. The full length of control rod range from -120 cm to zero is covered. As shown in the figure, the maximum prediction error is less than 2 cm.

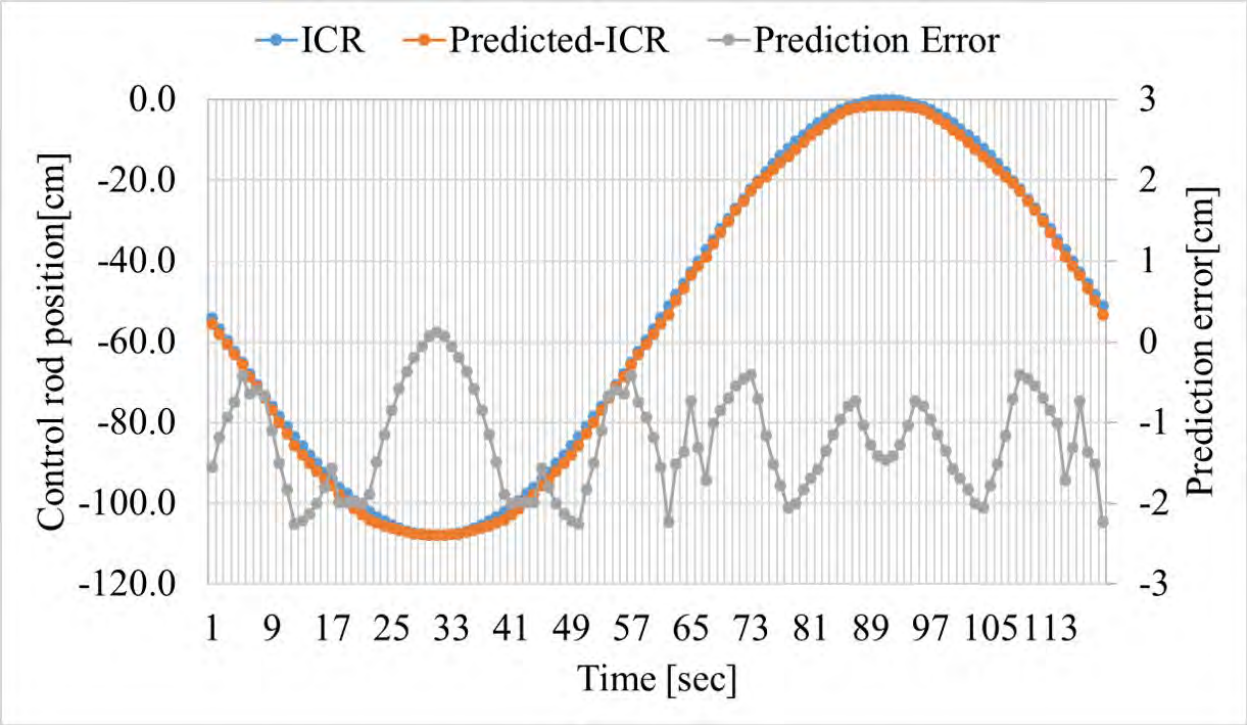

Figure 15: Optimized prediction results of the virtual control system.

4 MGEP Autonomous Control Demonstration

This section presents the experimental demonstration of the autonomous control system (ACS) designed for the MIT Graphite Exponential Pile (MGEP). The ACS was intended to autonomously respond to perturbations through linear actuation of control rods with neutron absorbers, which aims to keep the neutron flux profile symmetric after unknown control rods perturbations. An artificial neural network (ANN) was trained and used for decision making for the ACS. For the experimental demonstration, the real-world experiment was set up on the MGEP to demonstrate the functionality of ACS with integration of a Helium-3 (He-3) neutron detector and control rods including their moving devices. In the demonstration experiment, the perturbed flux profile was measured by the mobile Helium-3 neutron detector being placed in the desired graphite layer and scanning the length of the layer. The deep learning regression model was trained by the flux measurements taken before the demonstration. Finally, the prediction accuracy in the demonstration was presented and discussed to validate the viability of this autonomous control system for subcritical nuclear facility -- MGEP.

4.1 Hardware Setup

4.2 Hardware Operation

High-fidelity numerical modeling and simulation is the first step to investigate the neutronic characteristics of the MGEP before developing the data-driven control system (DCS). Figure 3 illustrates the front view of the MGEP, which is a graphite cube with 90 inches per side sitting on top of an underground graphite pedestal. A total of 1288 cylindrical fuel slugs are placed in 12 layers of graphite blocks in the North-to-South direction. In addition, another 12 layers of graphite blocks with void channels in the center support the measuring channels for neutron flux detector or control rod insertion in the east-to-west direction, namely layer "A" to layer "L" as shown in Figure 3.

As shown in Figure 3, a Pu-Be or Cf-252 source can be placed in the underground pedestal as an external neutron source to increase the neutron flux to an easily measurable level. As the neutron fluxes of interest are referenced relative to the graphite layers spanning from "F", "G", "I" and "J", neutron detectors are placed in these channels. The exact location of neutron detectors is adjusted to achieve optimal performance of neural network prediction models used in the control system. The previous work shown in previous sections indicates layer "I" has the most sensitive response corresponding to linear actuation of the dual control rods, which are placed in the layer "H". One of the dual control rods is used as the initiating control rod (ICR), which travels on the east half of the channel and perturbs the neutron flux. Another one is taken as the responding control rod (RCR), which covers the west half of the channel and restores the symmetric neutron flux. The moving range of ICR (right end of the active length) varies from -75.1 cm to -7.7 cm and the range of RCR (left end of the active length) changes from 7.7 cm to 75.1 cm. Correspondingly, the detector movable range (center of the active length) in layer "I" can be from -87.5 cm to 92.5 cm. The coordinate system adopted in this work is also displayed in Figure 3, with the origin located in the center of the graphite layer and the positive x-axis points along the east-to-west direction.

The framework of the experimental demonstration is shown in Figure 16. In this system, the regression model is extended from digital twin-based control system that was developed first as a proof of concept and discussed in previous sections. The exception for the experimental demonstration is that the training data sets are collected from a flux measuring experiment instead

of Monte Carlo simulation results. The kernel of this framework is LabVIEW with different interfaces, which drives TCP/IP interface for Helium-3 neutron detector control and data collection, and Python interface to execute NPSN-based neural network prediction, and also the LINX interface to control the control rods moving system and neutron detector moving system via the Arduino micro-controller board and the stepper motors.

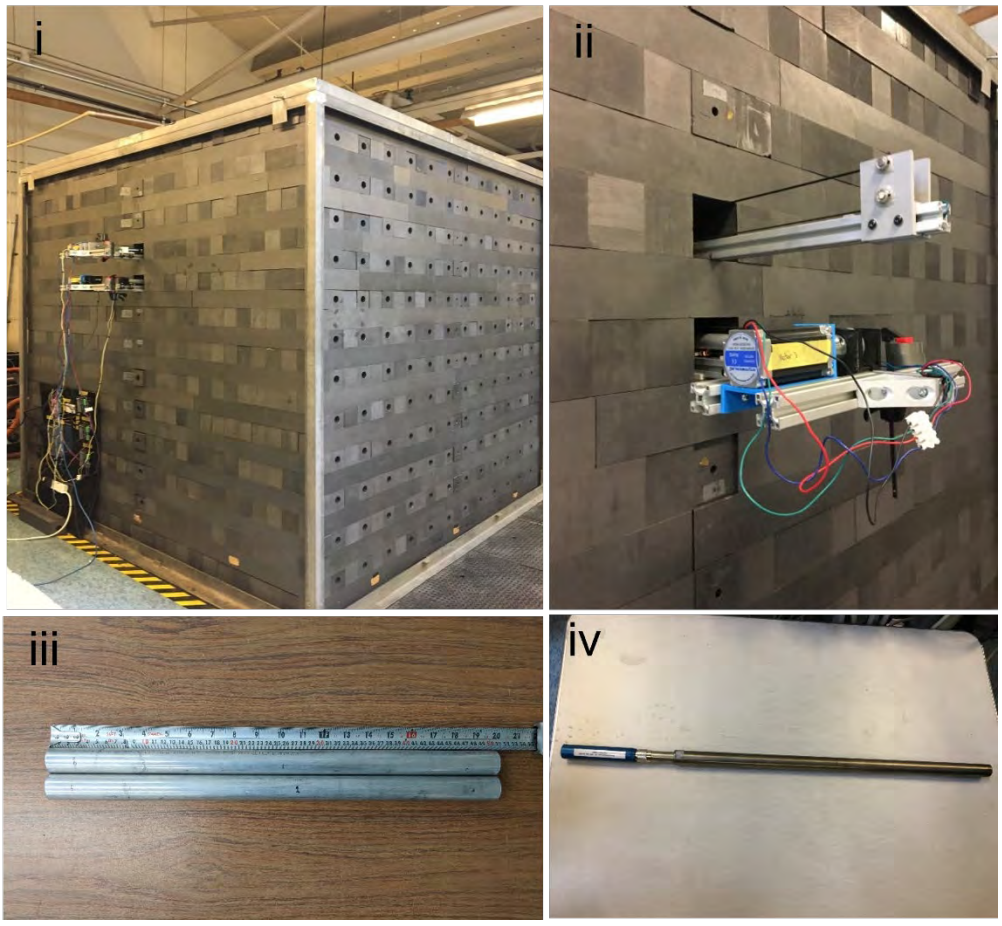

Figure 16: Experiment setup i) Overview of MGEP and two rails; ii) zoom-in view of two rails from west side; iii) two control rods; iv) He-3 detector and electronics device).

This work aims to develop a DCS for the MGEP to autonomously respond to unknown neutron flux perturbations. We introduce δS as the relative difference of the neutron flux profile along the x-axis between and left half and right half, which can be referred to as the figure of merit that is able to quantify the symmetry of flux profile, which can be expressed as follows,

$$\delta S = S_{left}/S_{right} - 1$$

Where,

$$S_{left} = \int_{-75.1}^{-7.7} \phi(x)\,dx \text{ and } S_{right} = \int_{7.7}^{75.1} \phi(x)\,dx$$

denote that flux integral under the left and right side of the flux profile respectively. The objective of this work is to minimize the δS by adopting the neural network regression model that correctly predicts the perturbed position of ICR, and automatically moving the RCR to a symmetric position.

4.3 Integration and Demonstration

The experimental data sets that are used to train neural network in the experimental demonstration are obtained from the He-3 neutron detector. The total of 144 permutation cases of dual control rods insertion, which is exactly the same with that generated for simulation data sets preparation. With the consideration of reducing measuring uncertainty to a significantly lower level (the measured background is approximately 25 counts per second), at least 60 seconds is required as the measuring time at each measuring location. Additionally, 15 cm is selected as the interval distance between two neighboring measuring locations, which lead to the measuring locations vary from 15 cm to 195 cm with the increment of 15 cm. To better determine the impact of different measuring time at each location on the neural network prediction performance, another experiment with 120 seconds as the measuring time is conducted to form the so-called high-resolution data set, whereas the former data set with 60 seconds of measuring time is named low-resolution data set.

Figure 17 presents the front panel (lower subplot) and logic panel (upper subplot) of the experimental autonomous control system, which is designed in LabVIEW programming language and then integrated with neutron detectors via TCP/IP interface. Labview also interfaces with an Arduino, or Raspberry Pi board based micro-controller to control the stepper motors. The stepper motors control the movement of detector for the neutron flux measurement, the dual control rods -- ICR and RCR. Note that both the detector and dual control rods are installed on the railings in the pile with movable stands and belts that have been driven by stepper motors. Different from the digital twin-based control system, this system directly collects the flux profile of the MGEP via detector moving system and detector signals post-processing. Moreover, the regression model is still adopted to provide real-time control rod prediction functionality. However, the regression model is previously trained by experimental data sets. The prediction error is used to assess the performance of this integrated experimental demonstration.

Figure 18 shows the logic for the control system response to a perturbation. Essentially the control system utilizes the neural network to estimate the position of the ICR and moves the RCR to the symmetric positions, it then reevaluates the estimated position and moves the RCR again until either it is moving less than the delta (typically 0.5 cm) or the max iteration counter has been reached (typically 3). Table 2 shows the optimized neural network parameters as used to train the regression model.

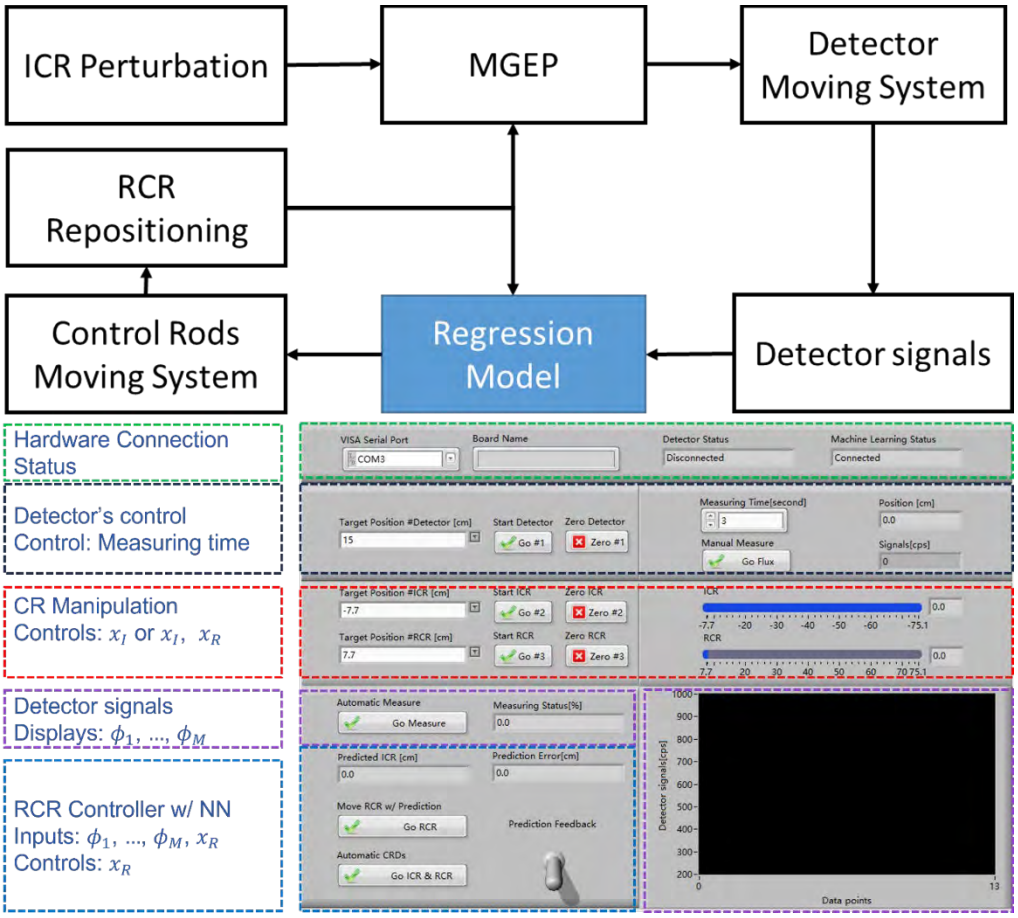

Figure 17: Logic framework (upper) and LabVIEW front panel (lower) of experimental autonomous control system.

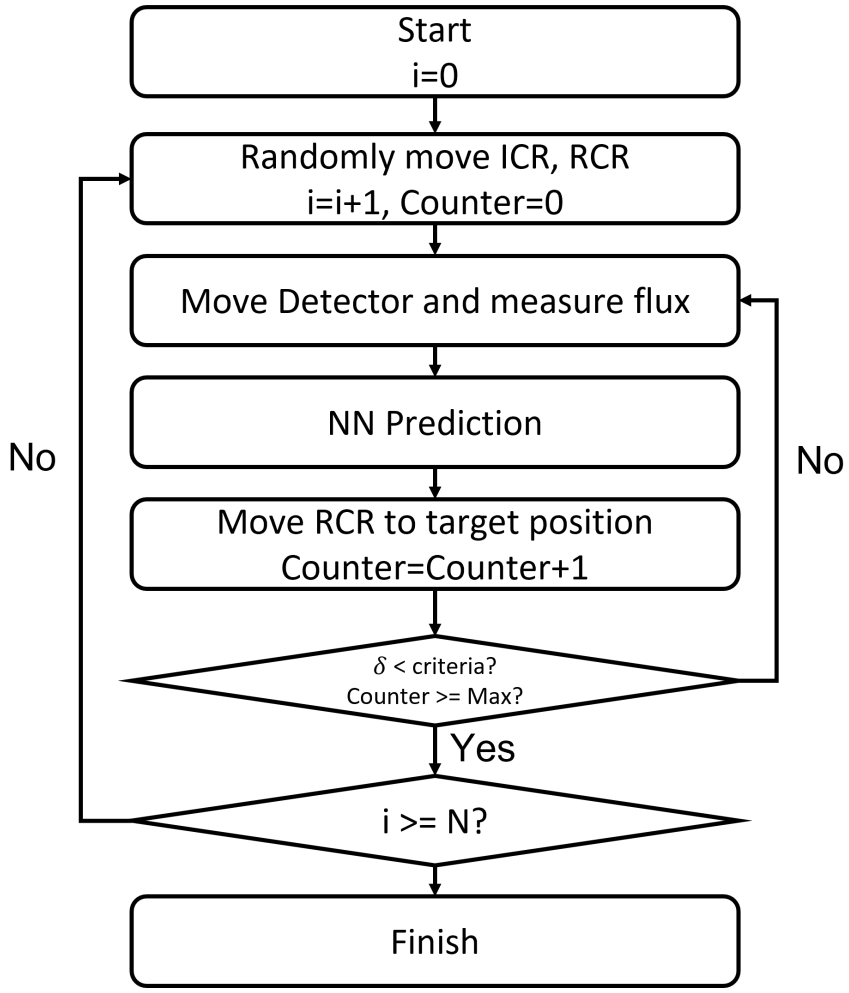

Figure 18: Flow chart of data-driven control system for moving MGEP control rods

4.4 Artificial Neural Network and Regression Model

The open-source artificial neural network (ANN) machine learning code toolkit – NPSN [8], [14] has been adopted and modified to build the neural network regression model. NPSN provides an abstracted path to creating models for multidimensional regression of neutron flux distribution based on control rod position(s) for any type of nuclear facility including critical and subcritical ones. The flow chart can be referred to the NPSN layout figure in the reference paper [8]. In general, a deep learning neural network model typically has one input layer, multiple intermediate dense layers, and one output layer. Note that users are required to match the dimension of input and output layer according to the detailed data sets. Take the regression model developed in this work as an example, the input is a one-dimensional array with the size of 14, which covers the single value for the RCR position and another 13 flux values at 13 measuring locations. The neural network regression model outputs only one single value that is the ICR's position.

The deep neural network regression model is built to determine the unknown control rod position prediction by analyzing the neutron flux profile measured from a Helium-3 neutron detector. The ANN model is instantiated and trained by NPSN. This package adopts Tensorflow [17] and Keras [18] to provide the high-level application programming interface (API). NPSN was initially

utilized to develop a neural network surrogate model for the MIT reactor (MITR) [19][20], but then was modified to model the MGEP [8].

The neural network regression models can be expressed as below,

$$f_{NN} \sim f(\phi(d_1, ..., d_M), x_{RCR}) = x_{ICR}^{predicted}$$

where x is the position of control rod, φ denotes the detector signals reflecting neutron flux of the graphite pile, and M is the maximum number of experimental data points. To quantify the model's performance, the prediction error in the regression model is calculated as below,

$$\delta_{NN} = x_{ICR}^{predicted} - x_{ICR}^{actual}$$

where δ_{NN} represents the prediction error of control rod perturbation in the regression model.

4.5 Demonstration Results and Discussion

An example of the operation of the autonomous control system and the resulting neutron flux is shown in Figure 19, where the ICR is moved to a location unknown to the autonomous control system of -25.0 cm. The detector then scans the pile in 15 cm increments to determine the neutron flux profile. The ANN then predicts the location of the ICR, in this case it predicts a position of -26.3 cm, an error of 1.3 cm. The system then moves the RCR to the symmetric position of 26.3 cm to bring the flux back to a symmetric profile. Figure 19 shows the response of the neutron flux as the RCR is moved to the symmetric position.

The aggregate demonstration results and the associated error for all cases is presented in Figure 20, where the upper subplot illustrates the prediction performance with regression model that is trained by low-resolution experimental data set, and the lower subplot expresses the prediction error with regression model trained by high-resolution date set. The maximum prediction error was significantly reduced from 7 cm to 4 cm. The experimental results for 13 cases are shown in Table 5, which shows the value of the flux asymmetry after the system responds to the ICR movement. The ICR and RCR positions are given in cm utilizing the coordinate system shown in Figure 3. The initial δS is from the movement of the ICR, the final δS is after the RCR responds, and the reference δS is from the ANN trained on the digital twin high fidelity neutronic simulations.

Figure 21 shows the results from the highly trained optimized digital twin as discussed in previous sections. The results on this case perform even better than the experimental cases as there are no experimental complications of position, material, or geometric uncertainties.

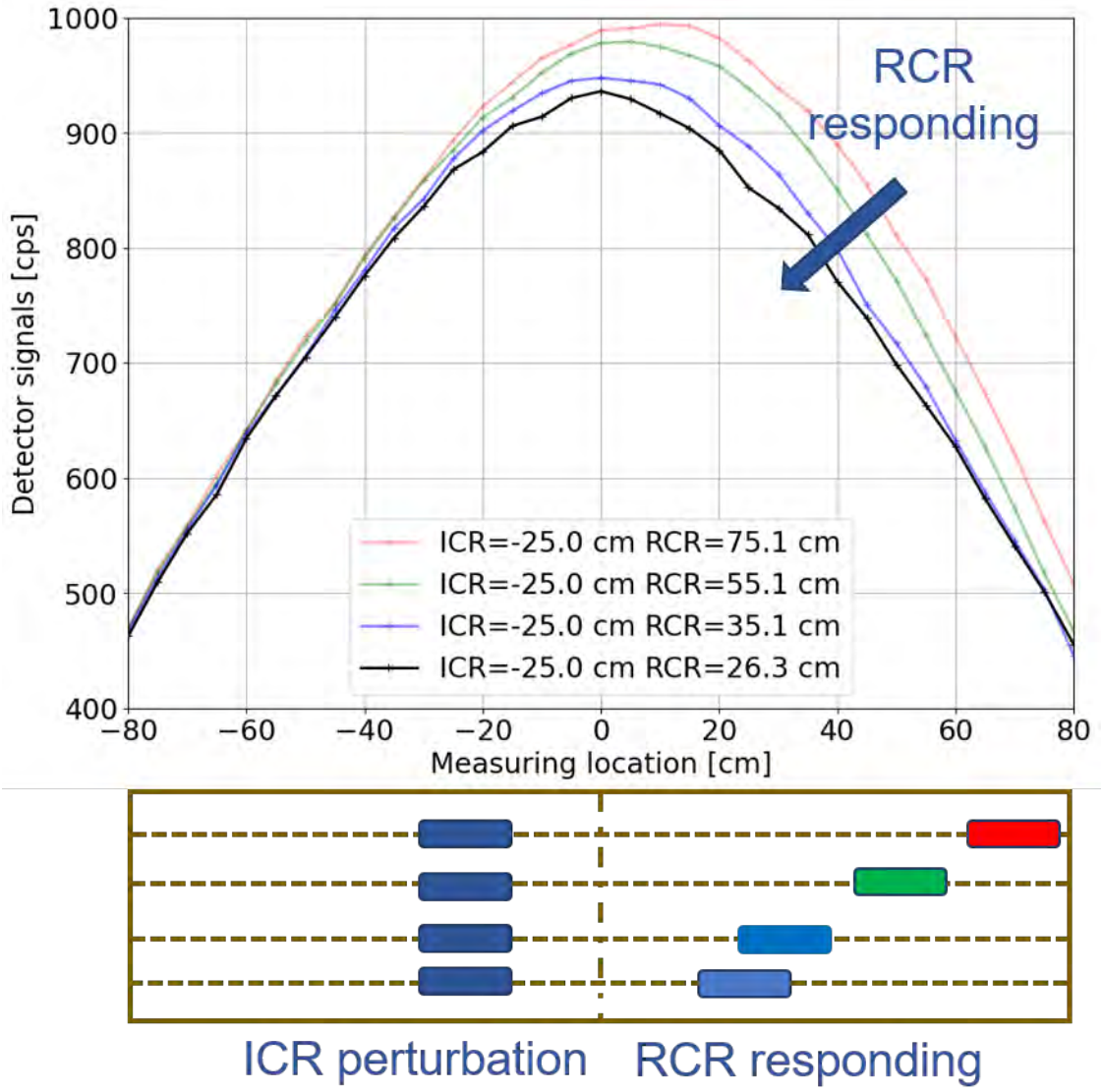

Figure 19: Top graphic shows the flux profile changing as the RCR responds to the symmetric position shown in the lower graphic.

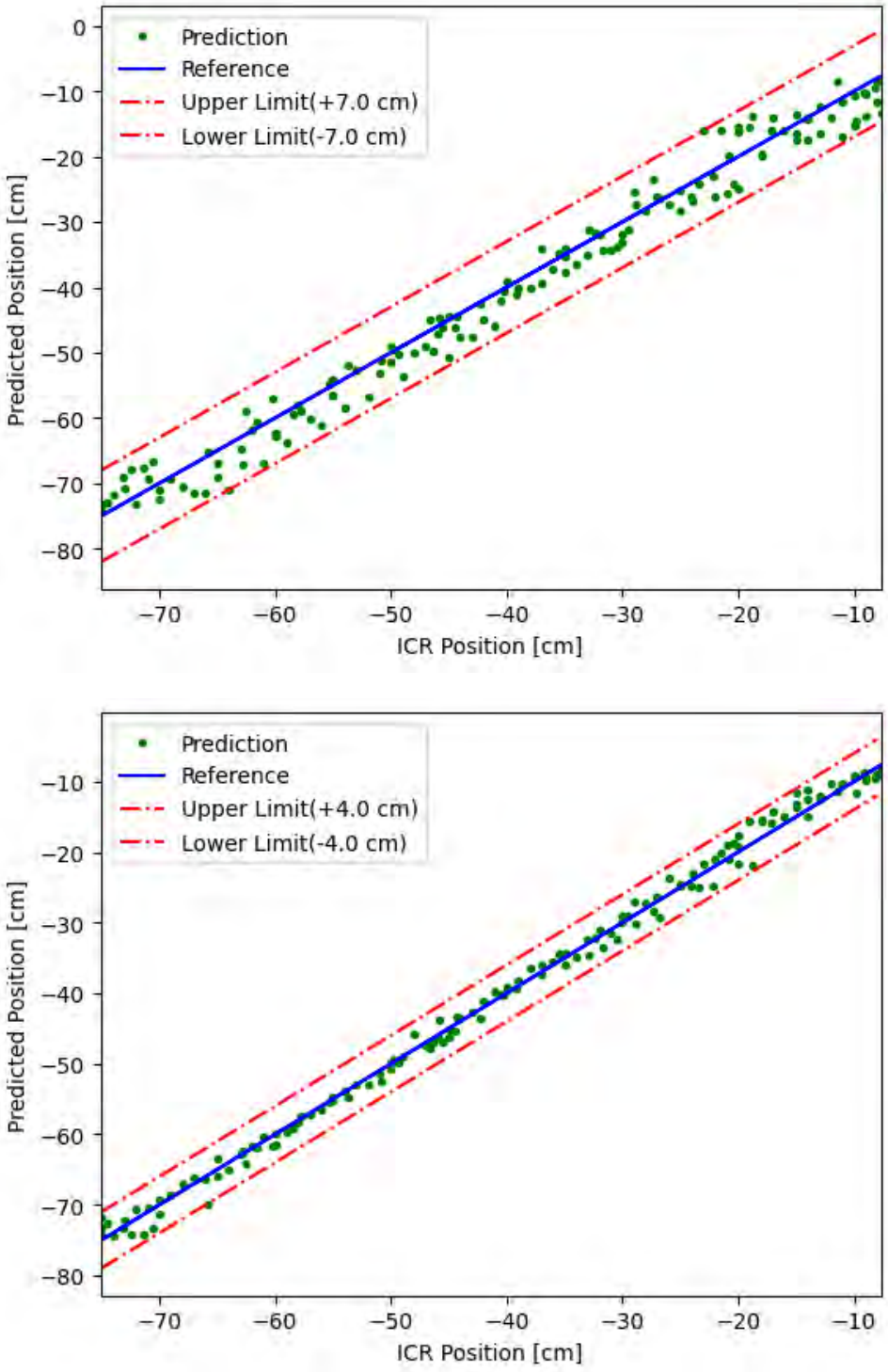

Figure 20: Prediction results of experimental control system with low-resolution time data (upper) and high-resolution time data (lower).

Table 5: Integral experimental demonstration of control system performance

Case No.	Initial ICR	Initial RCR	Final RCR	Initial δS	Final δS	Reference δS
1	-10.0	75.1	11.0	-13.2%	-0.54%	-0.09%
2	-15.0	75.1	16.5	-13.7%	-0.61%	-0.41%
3	-20.0	75.1	19.2	-6.95%	-0.72%	-0.41%
4	-25.0	75.1	23.9	-7.60%	-0.49%	-0.32%
5	-30.0	75.1	28.8	-4.70%	-0.86%	-0.67%
6	-35.0	75.1	34.2	-3.27%	-1.16%	-0.79%
7	-40.0	75.1	40.6	-2.31%	-0.77%	-0.82%
8	-45.0	75.1	43.9	-3.18%	-0.76%	-0.92%
9	-50.0	75.1	48.9	-4.28%	-0.77%	-0.87%
10	-55.0	75.1	57.0	2.67%	0.82%	-0.73%
11	-60.0	75.1	61.5	1.10%	-0.82%	-0.71%
12	-65.0	75.1	64.7	0.91%	-0.77%	-0.58%
13	-70.0	75.1	71.7	0.92%	-0.77%	-0.58%

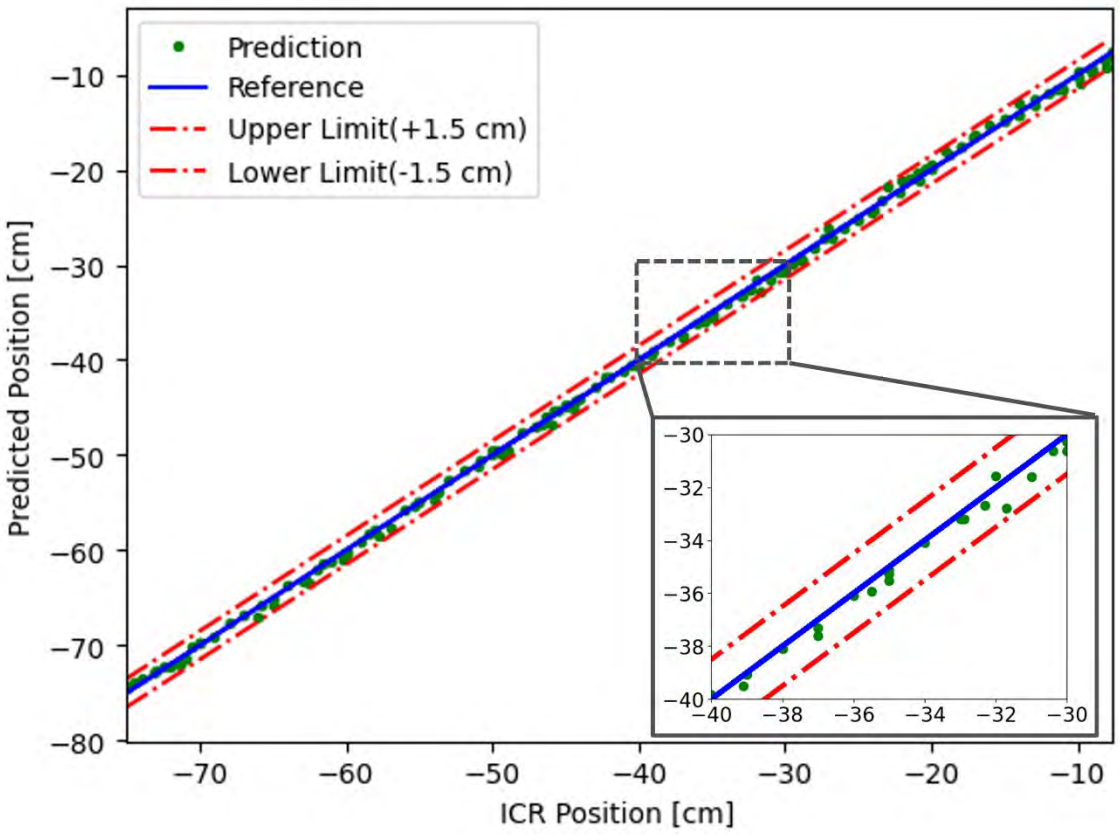

Figure 21: Predication performance of regression model trained by high-fidelity simulation data

5 Fault Tolerance

Prior work discussed previously performed on the MGEP trained neural networks using simulated (modeling) data and detector data to predict ICR positions given a flux profile and the known position of the RCR. The quality of the data acquired by the sensors is essential to the accuracy of the neural networks trained on those data sets. Consequently, fault tolerance methods must be implemented to verify sensor functioning and make sure any outliers are properly handled.

Fault tolerance is the method in which faults are appropriately identified and resolved to ensure that the system continues to function as intended. Previous research in the field has led to several proposed methods of outlier detection. In both [21] and [22], principal component analysis (PCA) is suggested as a method of creating a data driven model, while in [23] anomalies are detected through Hotelling's T2 test and interquartile range (IQR). In [24], Banerjee et al. creates an artificial neural network (ANN) to detect sensor faults through a combination of sigmoid activation functions, mean squared error (MSE) loss and regression analysis.

Other dimensionality reduction techniques (like PCA) include t-Distributed Stochastic Neighbor Embedding (t-SNE), which utilizes Gaussian and Student t-distributions to create clusters of related data [25]. Certain neural networks used for classification, like convolutional neural networks (CNN), tend to process images and areas particularly well [26], while others, like k-Nearest Neighbors (kNN), focus on the distance between an unclassified point and surrounding, labeled data to classify it [27]. Thus, t-SNE data can be visualized for CNN application and fed directly into a kNN algorithm. This work develops outlier detection methods to identify sensor failures in the MGEP through the combination of several of the aforementioned techniques and evaluates the accuracy of each procedure.

5.1 Methods

5.1.1 Fault Insertions

Our datasets are initially arranged in a 144 x 14 matrix, with the rows indicating the trial number, columns 1 through 13 containing the flux reading at a particular position, and column 14 containing the RCR position value for that trial.

Faulty data is generated by calculating the standard deviation of each detector data column and ensuring that the faults created are at least 2 deviations (σ) away from the mean (μ). These faults are then randomly placed within their corresponding detector data columns. The faults are only generated for the flux readings, and not the RCR values.

5.1.2 PCA and IQR

For the PCA and IQR method, the RCR values have been dropped, resulting in a starting matrix of dimensions 144 x 13 for both the modeling and detector datasets.

PCA first reduces a matrix from $d+1$ dimensions to d by removing labels associated with the dataset. When PCA is applied to the MGEP modeling dataset, the dimensions stay the same as the labels have not been included. Next, the mean of each data column is calculated and the covariance matrix of the dataset is computed through the equation,

$$cov(X,Y) = \frac{1}{n}\sum_{i=1}^{n}(x - \bar{x})(y - \bar{y})$$

where x and y represent the variables and $\bar{x}, \bar{y}$ represent the mean. The covariance results in a square matrix of $d\ by\ d$ dimensions whose eigenvectors and eigenvalues can be calculated. The final dimensions produced by PCA are $d\ by\ k$, where k is the number of important features used to explain the variance in the data, selected in descending order from the greatest eigenvalue. For the MGEP, three features have been selected. After extracting the features from the modeling dataset and transforming the faulty detector data, outlier experiments are removed through Hotelling's T^2 test

$$T^2 = n(\bar{x} - \mu_0)S^{-1}(\bar{x} - \mu_0)$$

where n random samples are selected to create a covariance matrix S, $\bar{x}$ is the mean of the sample, and μ_0 is the mean of the original data. When $\bar{x} \approx \mu_0$, the T^2 value approaches 0. By choosing an appropriate threshold for T^2, outlier experiments can be selected and removed to refine the dataset and IQR can be applied to find the data point(s) responsible for the high T^2 value. IQR works by finding the range where the middle 50% of the data lies, which is then multiplied by some constant c and added the first (Q_1) and third (Q_3) quartiles to create the upper and lower bounds of accepted values:

$$Q_3 - Q_1 = IQR$$

$$Bound_{upper} = Q_3 + c * IQR$$

$$Bound_{lower} = Q_1 - c * IQR.$$

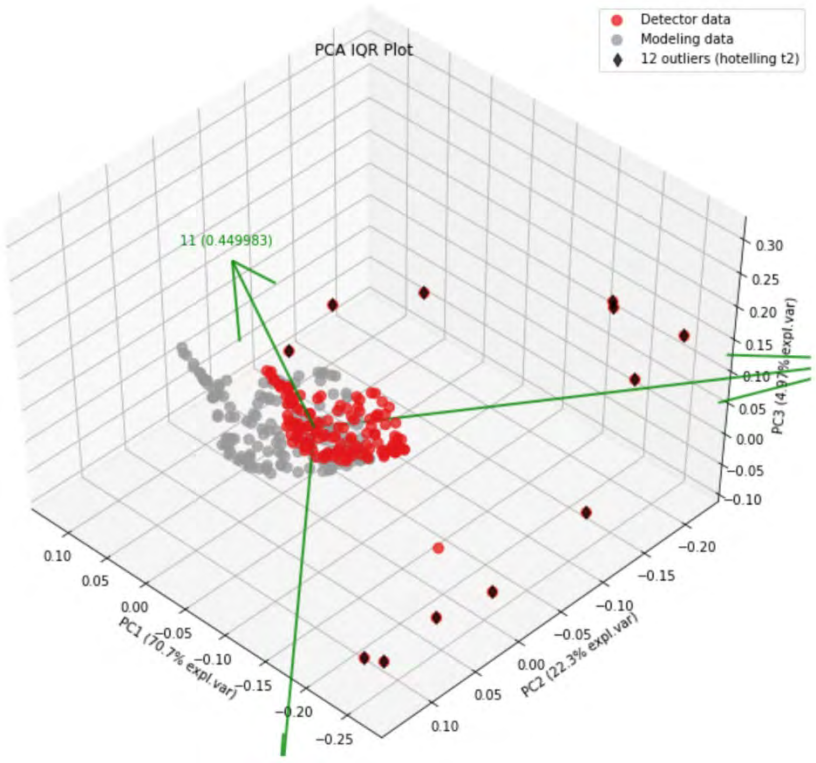

Figure 22: PCA IQR data plotted along the three principle components.

Through testing, the value of c has been set to 1.6 for the MGEP. An example of the data is shown in Figure 22. The plot is generated after using PCA on modeling data (gray dots) to extract principal components (PC) and applying them to the detector data (red dots). The green arrows are each PC, with the amount of variance in the data that they account for. The axes represent the PCs in a cartesian coordinate system. Because the modeling and detector data have the same general distribution, applying the PCs from the modeling data onto the detector data will result in similar shapes, but the value differences will shift their locations, as shown in Figure 22. Points that do not match the distribution (outliers) will be significantly affected by the modeling PCs and will be located far from the main cluster. Outlier rows detected by PCA through Hotelling's T^2 test are indicated by black diamonds. These outlier rows will then be removed from the dataset and IQR is applied to find the point that is the source of the error.

5.1.3 T-SNE and kNN

The next method explored is the combination of t-SNE and kNN. Like PCA, t-SNE also reduces data dimensionality, however, it does so through a combination of distributions. The data is reduced from an array of size $a\ x\ b$ to $a\ x\ n$, where n is a specified number of components.

First, a Gaussian distribution is applied to an $a\ x\ b$ array

$$p_{j|i} = \frac{\exp(\frac{-||x_i - x_j||^2}{2\sigma_i^2})}{\sum_{k \neq i} \exp(\frac{-||x_i - x_k||^2}{2\sigma_i^2})}.$$

Where all of the possible pair-wise interactions are considered. To set the appropriate σ value, perplexity is used, which is defined as:

$$Perplexity(p_i) = 2^{-\sum_i p_{j|i} log_2(p_{j|i})}.$$

The results are then symmetrized through

$$p_{ij} = \frac{p_{j|i} + p_{i|j}}{2}.$$

Additionally, Student's t-distribution is applied to the original dataset

$$q_{ij} = \frac{(1 + ||y_i - y_j||^2)^{-1}}{\sum_{k \neq l}(1 + ||y_k - y_l||^2)^{-1}}.$$

Next, Kullback-Leibler (KL) divergence is applied to make the distributions as similar as possible.

$$C = \sum_{ij} p_{ij} log \frac{p_{ij}}{q_{ij}}.$$

The gradient of KL divergence is then used as a cost function to minimize the differences between the probability distributions.

Afterwards, KNN is applied. First, a distance metric is selected, which has been set to the Euclidian metric for the MGEP. Next, each point x is assigned to a class with the largest probability based on its location

$$P(y = j|X = x) = \frac{1}{K}\sum_{i \in A} I(y^{(j)} = j).$$

The K-value impacts the number of neighbors considered when classifying x. For larger values, more data is considered and generally makes it more tolerant to outliers. Smaller K will focus more on the local distribution, and looks at a smaller region surrounding the point.

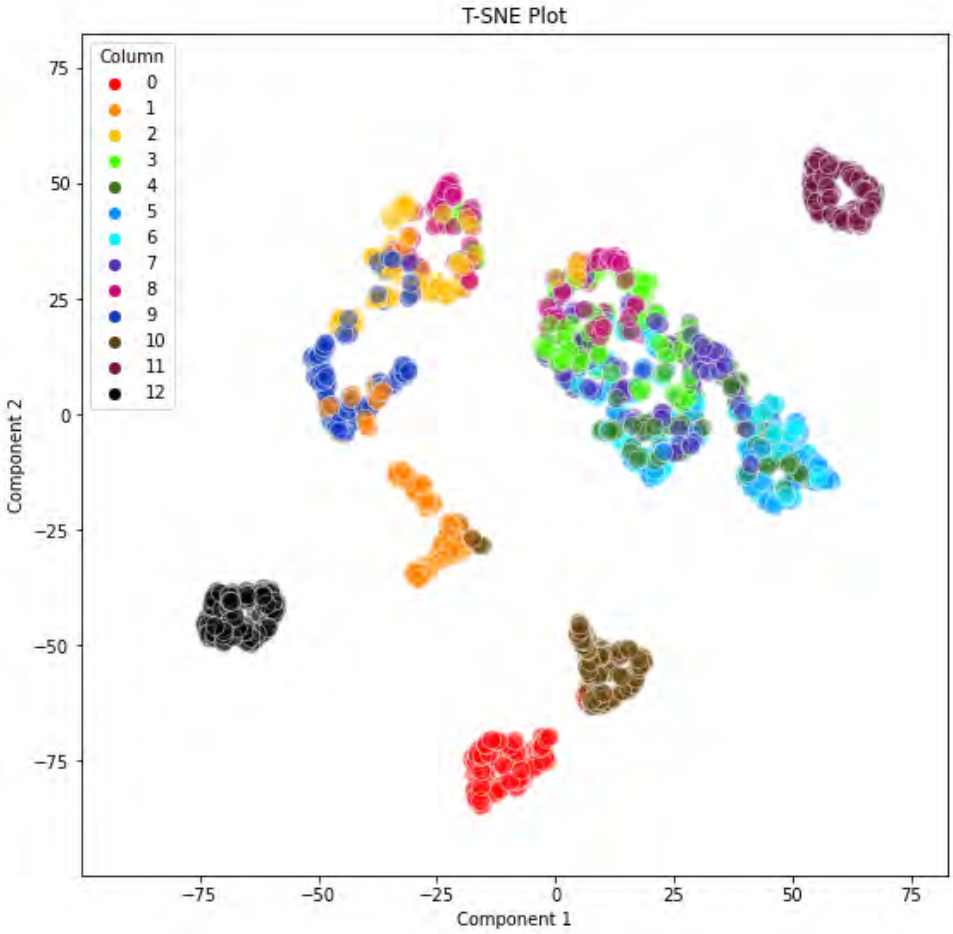

Figure 23: T-SNE data plotted along principle components.

An example of data after being transformed by T-SNE data from the MGEP is shown in Figure 23. In t-SNE, components are extracted to find relationships between data points. Points that are more related to each other tend to be clustered together.

For Figure 23, each of the columns of data (144 rows x 13 columns) have been clustered into groups. The axes indicate the components extracted from applying t-SNE.

The image shows that the data points are most related to the column they belong to. Columns 3 through 7 contain similar data distributions, while some others are loosely related, and columns 0, 10, 11 and 12 are mostly or completely independent. This indicates that when searching for outliers, focusing on the relation of a data point to other column members may be more effective than comparing it to other points along its row.

Because convolutional neural networks (CNN) are able to work with area detection, these images can be fed into a CNN to extract important area features that will classify a column as inlier or outlier. The data arrays for each column can also be used in k-Nearest Neighbors (KNN), which will determine if a point is an inlier or outlier based on how far it is from nearby data points (neighbors).

5.1.4 T-SNE and CNN

Images generated using the t-SNE dataset can be fed into a convolutional neural network (CNN). They work by taking labels and images of specified dimensions, and then using a kernel to scan the image and extract important features. These features are then used to classify images.

Several layers include hyperparameters that can be tuned to increase the classification accuracy. Padding layers can expand the image matrix data by adding zeros, and pooling layers can extract the most relevant features while discarding noise. At the end of a CNN, a classification layer is added to categorize the images.

For the MGEP, the column data images are classified into acceptable and outlier categories.

Figure 24: CNN Feature plot.

In Figure 24 GradCAM, a gradient weighted class activation algorithm, has been applied on a CNN trained with t-SNE data to verify that it is identifying the correct features to label data as inliers or outliers. The top section shows the original t-SNE column data graph, containing a clear outlier (the lone point towards the bottom). The middle section shows the feature map, while the bottom overlays the feature map on the original image.

The image shown above shows that the CNN is successfully learning that the data points are the features that are important for accurate classification (highlighted in yellow) while

generally disregarding the white space of the graph (indicated by the red). This ensures that the CNN model is functioning as intended.

5.2 Fault Tolerance Results

In all methods, the accuracy is measured as the number of correct fault points removed divided by the number of faults inserted.

TABLE I. Method Accuracy

Method of Evaluating Fault	Fault Detection Accuracy
PCA + IQR	95%
T-SNE + KNN	68.5%
T-SNE + CNN	75%

The PCA + IQR method resulted in a 95% accuracy, while t-SNE + KNN and t-SNE + CNN had a 68.5% and 75% accuracy, respectively (summarized in Table 1).

6 Conclusions

A virtual control system has been developed to theoretically verify the practicality of the technical road map. It has three major components to build the framework of the virtual control system with LabVIEW graphical programming language with Python interfaces, including control rod manipulation, detector signal generator and control rod prediction and feedback. The neural networks behind detector signal generator and control rod prediction modules are trained by the machine learning algorithms with the training data sets generated by high-fidelity Monte Carlo neutron transport modeling and simulation. It has proven that the virtual control system has the control rod prediction error less than 2 cm.

The experimental autonomous control system was designed, fabricated, and installed in the MGEP. The system has been integrated using three major components including the helium-3 neutron detector with its data collection device, neural network-based control rod prediction module, and the control rods manipulation device.

The autonomous control system is mainly designed in LabVIEW with Python and the necessary hardware integration of the He-3 neutron detector, the Arduino/Raspberry Pi, and stepper motor control of the control rods and neutron detector. The neural network behind the control rod prediction module is trained by the measured neutron flux data from the detectors via the calibrated in-pile experiment with various control rods perturbations. The experimental demonstration showed the prediction error of experimental autonomous control system is less than 4.0 cm. The

limitation of further reduction of prediction error is likely inherent to the experimental setup based on the accuracy of the equipment. One way to improve this further would be to use a He-3 detector with higher spatial resolution as well as control rods with higher worth to increase the sensitivity of the system.

This work actively demonstrates an innovative DCS that can be viable in a subcritical nuclear facility by adopting a neural network-based machine learning algorithm, micro-controller driven hardware, and a LabVIEW based system integration. It introduces experimental data sets in neural network training and integrates them in the control system final demonstration, which mitigates the deficiency in many DCS systems that only adopt modeling and simulation data sets. However, there are some limitations in this work, such as the total time spent in moving the detector and taking measurements is high due to the low count rates in a subcritical pile. This drawback can be mitigated by using a neutron detector with spatial sensitivity, the use of multiple detectors, or testing on a system with a higher neutron flux. Also, the flux profile is not the objective function, but the ICR position is predicted, and then the RCR is moved to the symmetric location which also restores flux symmetry based on the geometric symmetry of the pile. Using the flux profile as the objective function could be more of an analog to a critical system and explored in future work.

Fault tolerance of the system was also investigated and several different techniques were employed to determine the best methods for optimal fault tolerance of the system. Faults were introduced with an erroneous signal that is outside 2 standard deviations of the data scatter for that point. PCA+IRQ methods were able to identify the outlier with 95% accuracy, the modeling data was then used to fill in the data hole. These results show that Fault tolerance methods can be employed to improve the function of an DCS.

Overall the project successfully implemented an autonomous control system both using a digital twin of the MGEP and a physical DCS on the actual MGEP. The digital control system was able to predict the location of an unknown movement of a control rod (ICR) and move another control rod (RCR) to a symmetric position. The symmetry of the flux was shown to be within just a little over 1% after the RCR response. Fault tolerance methods were also employed to demonstrate the robustness of the system to faulty data inputs.

7 References

[1] "The Future of Nuclear Energy in a Carbon-Constrained World | MIT Energy Initiative." https://energy.mit.edu/research/future-nuclear-energy-carbon-constrained-world/ (accessed Dec. 29, 2022).

[2] R. T. Wood, B. R. Upadhyaya, and D. C. Floyd, "An autonomous control framework for advanced reactors," *Nucl. Eng. Technol.*, vol. 49, no. 5, pp. 896–904, Aug. 2017, doi: 10.1016/J.NET.2017.07.001.

[3] N. M. Upadhyaya BR, Zhao K, Perillo SR, Xu X, "Autonomous control of space reactor systems," 2007.

[4] L. Lin *et al.*, "Development and assessment of a nearly autonomous management and control system for advanced reactors," *Ann. Nucl. Energy*, vol. 150, p. 107861, Jan. 2021, doi: 10.1016/J.ANUCENE.2020.107861.

[5] L. Lin *et al.*, “Digital-twin-based improvements to diagnosis, prognosis, strategy assessment, and discrepancy checking in a nearly autonomous management and control system,” *Ann. Nucl. Energy*, vol. 166, p. 108715, Feb. 2022, doi: 10.1016/J.ANUCENE.2021.108715.

[6] M. D. (Micah D. Gale, “Developing modern graphite exponential pile experiments to augment reactor physics education,” 2018, Accessed: Dec. 29, 2022. [Online]. Available: https://dspace.mit.edu/handle/1721.1/119041.

[7] S. E. . Hauptman, “Characterization of the MIT Graphite Exponential Pile,” 2019, Accessed: Dec. 29, 2022. [Online]. Available: https://dspace.mit.edu/handle/1721.1/123366.

[8] A. J. Dave, J. Wilson, and K. Sun, “Deep Surrogate Models for Multi-dimensional Regression of Reactor Power,” pp. 737–740, Jul. 2020, Accessed: Sep. 27, 2021. [Online]. Available: https://arxiv.org/abs/2007.05435v2.

[9] N. A. ,S. M. M. I. of T. Costa, “Physical specifications and measurements of the MIT Graphite Exponential Pile,” 2020, Accessed: Dec. 29, 2022. [Online]. Available: https://dspace.mit.edu/handle/1721.1/127302.

[10] A. J. Dave, J. Yu, J. Wilson, B. Phillips, K. Sun, and B. Forget, “Empirical Models for Multidimensional Regression of Fission Systems,” May 2021, Accessed: Sep. 22, 2021. [Online]. Available: https://arxiv.org/abs/2105.14645v1.

[11] J. C. . Wilson, “Machine learning for nuclear fission systems : preliminary investigation of an autonomous control system for the MGEP,” 2019, Accessed: Dec. 29, 2022. [Online]. Available: https://dspace.mit.edu/handle/1721.1/123363.

[12] J. Yu, J. Wilson, B. Phillips, and A. Dave, “Development of a Virtual System in Support of Demonstrating Autonomous Control of a Subcritical Facility,” NPIC/HMIT-2021, ANS Virtual Meeting, 2021. doi: 10.13182/t124-34211.

[13] J. Yu, J. Wilson, B. Forget, A. J. Dave, K. Sun, and B. Phillips, “Experimental validation of a high fidelity Monte Carlo neutron transport model of the MIT graphite exponential pile,” *Prog. Nucl. Energy*, vol. 152, p. 104368, Oct. 2022, doi: 10.1016/J.PNUCENE.2022.104368.

[14] A. Dave, “NPSN: Nuclear Power Surrogate Network.” https://github.com/a-jd/npsn/.

[15] J. Wilson, J. Yu, B. Phillips, and A. J. Dave, “Development of an In-Pile Facility to Demonstrate Autonomous Control of a Subcritical System,” NPIC/HMIT-2021, ANS Virtual Meeting, 2021.

[16] P. K. Romano, N. E. Horelik, B. R. Herman, A. G. Nelson, B. Forget, and K. Smith, “OpenMC: A state-of-the-art Monte Carlo code for research and development,” *Ann. Nucl. Energy*, vol. 82, pp. 90–97, Aug. 2015, doi: 10.1016/J.ANUCENE.2014.07.048.

[17] M. Abadi *et al.*, “TensorFlow: Large-Scale Machine Learning on Heterogeneous Distributed Systems,” Mar. 2016, doi: 10.48550/arxiv.1603.04467.

[18] “Keras: the Python deep learning API.” https://keras.io/ (accessed Dec. 29, 2022).

[19] A. J. Dave, K. Sun, L. wen Hu, S. H. Pham, E. H. Wilson, and D. Jaluvka, “Thermal-hydraulic analyses of MIT reactor LEU transition cycles,” *Prog. Nucl. Energy*, vol. 118, p. 103117, Jan. 2020, doi: 10.1016/J.PNUCENE.2019.103117.

[20] K. Sun, L. W. Hu, and C. Forsberg, “Neutronics feasibility of an MIT Reactor–driven subcritical facility for the Fluoride-salt–cooled High-temperature Reactor,” *Int. J. Energy Res.*, vol. 41, no. 14, pp. 2248–2257, Nov. 2017, doi: 10.1002/ER.3786.

[21] N. Kaistha and B. R. Upadhyaya, “Incipient Fault Detection and Isolation of Field Devices in Nuclear Power Systems Using Principal Component Analysis,” *http://dx.doi.org/10.13182/NT01-A3240*, vol. 136, no. 2, pp. 221–230, 2017, doi: 10.13182/NT01-A3240.

[22] B. R. Upadhyaya, K. Zhao, and B. Lu, “Fault monitoring of nuclear power plant sensors and field devices,” *Prog. Nucl. Energy*, vol. 43, no. 1–4, pp. 337–342, Jan. 2003, doi: 10.1016/S0149-1970(03)00046-5.

[23] T. H. Lin and S. C. Wu, “Sensor fault detection, isolation and reconstruction in nuclear power plants,” *Ann. Nucl. Energy*, vol. 126, pp. 398–409, Apr. 2019, doi: 10.1016/J.ANUCENE.2018.11.044.

[24] S. Banerjee, J. Deng, C. Gorse, V. Vajpayee, V. Becerra, and S. R. Shimjith, “ANN Based Sensor and Actuator Fault Detection in Nuclear Reactors,” *2020 8th Int. Conf. Control. Mechatronics Autom. ICCMA 2020*, pp. 88–94, Nov. 2020, doi: 10.1109/ICCMA51325.2020.9301579.

[25] K. Bunte, S. Haase, M. Biehl, and T. Villmann, “Stochastic neighbor embedding (SNE) for dimension reduction and visualization using arbitrary divergences,” *Neurocomputing*, vol. 90, pp. 23–45, Aug. 2012, doi: 10.1016/J.NEUCOM.2012.02.034.

[26] S. Albawi, T. A. Mohammed, and S. Al-Zawi, “Understanding of a convolutional neural network,” *Proc. 2017 Int. Conf. Eng. Technol. ICET 2017*, vol. 2018-January, pp. 1–6, Mar. 2018, doi: 10.1109/ICENGTECHNOL.2017.8308186.

[27] Z. Zhang, “Introduction to machine learning: k-nearest neighbors,” *Ann. Transl. Med.*, vol. 4, no. 11, Jun. 2016, doi: 10.21037/ATM.2016.03.37.

8 Appendix A: Permutations of the ICR and RCR positions used for training.

Case No.	ICR	RCR	Case No.	ICR	RCR	Case No.	ICR	RCR
1	-75.1	75.1	49	-9.0	52.0	97	-28.0	52.6
2	-21.5	12.4	50	-11.0	70.0	98	-29.0	13.2
3	-29.5	39.0	51	-13.0	27.0	99	-30.0	24.9
4	-9.1	46.3	52	-14.0	75.0	100	-31.0	56.5
5	-32.3	35.0	53	-15.0	20.0	101	-32.0	9.8
6	-24.1	73.5	54	-18.0	43.0	102	-33.0	36.9
7	-20.4	22.7	55	-20.0	38.0	103	-34.0	74.1
8	-55.3	53.3	56	-7.7	7.7	104	-35.0	59.3
9	-39.1	59.6	57	-10.0	10.0	105	-36.0	40.2
10	-35.0	70.2	58	-15.0	15.0	106	-37.0	58.5
11	-53.7	27.3	59	-20.0	20.0	107	-38.0	49.9
12	-11.4	52.4	60	-25.0	25.0	108	-39.0	38.6
13	-8.1	51.0	61	-30.0	30.0	109	-40.0	28.2
14	-62.8	59.0	62	-35.0	35.0	110	-41.0	63.7
15	-62.6	17.6	63	-40.0	40.0	111	-42.0	50.3
16	-14.0	66.0	64	-45.0	45.0	112	-43.0	31.4
17	-46.6	61.1	65	-50.0	50.0	113	-44.0	64.6
18	-9.9	68.7	66	-55.0	55.0	114	-45.0	34.8
19	-58.5	40.6	67	-60.0	60.0	115	-46.0	19.1
20	-27.3	48.7	68	-65.0	65.0	116	-47.0	57.3
21	-50.8	64.3	69	-70.0	70.0	117	-48.0	40.3
22	-60.2	14.5	70	-75.0	75.0	118	-49.0	17.0
23	-42.3	47.9	71	-61.6	48.1	119	-50.0	54.6
24	-40.3	55.6	72	-45.8	7.9	120	-51.0	27.3
25	-71.3	16.9	73	-20.8	67.5	121	-52.0	70.0
26	-65.8	30.8	74	-74.5	34.9	122	-53.0	59.2
27	-37.0	72.9	75	-40.5	10.8	123	-54.0	17.3
28	-22.2	74.4	76	-7.7	34.2	124	-55.0	38.7
29	-23.4	50.2	77	-8.0	10.3	125	-56.0	38.6
30	-32.9	39.9	78	-9.0	60.0	126	-57.0	26.0
31	-30.4	31.7	79	-10.0	48.7	127	-58.0	33.7
32	-44.5	21.1	80	-11.0	71.1	128	-59.0	69.8
33	-31.7	21.9	81	-12.0	55.9	129	-60.0	61.2
34	-49.4	15.9	82	-13.0	73.2	130	-61.0	26.9
35	-18.8	45.0	83	-14.0	10.9	131	-62.0	70.0
36	-72.5	56.0	84	-15.0	25.9	132	-63.0	26.3
37	-70.5	69.2	85	-16.0	40.9	133	-64.0	33.3
38	-26.8	15.0	86	-17.0	41.6	134	-65.0	22.1
39	-17.1	43.2	87	-18.0	14.7	135	-66.0	21.7
40	-45.5	71.8	88	-19.0	10.8	136	-67.0	72.7
41	-46.3	39.3	89	-20.0	25.0	137	-68.0	44.1
42	-73.2	54.8	90	-21.0	48.4	138	-69.0	28.3
43	-35.5	61.3	91	-22.0	11.1	139	-70.0	74.6
44	-57.8	23.2	92	-23.0	9.6	140	-71.0	11.9
45	-28.9	65.6	93	-24.0	59.1	141	-72.0	26.2
46	-44.3	38.5	94	-25.0	34.4	142	-73.0	55.7
47	-49.7	55.1	95	-26.0	35.0	143	-74.0	52.7
48	-8.0	19.0	96	-27.0	8.2	144	-75.1	62.4